Fundamental flow-path design, optimization and numerical analysis of flow in axial turbines

Hu, Heng

2025

Document Version:
Publisher's PDF, also known as Version of record

Fundamental Flow-Path Design

Optimization and Numerical Analysis of Flow in Axial Turbines

HENG HU
DEPARTMENT OF ENERGY SCIENCES | FACULTY OF ENGINEERING | LUND UNIVERSITY

Fundamental Flow-Path Design, Optimization and Numerical Analysis of Flow in Axial Turbines

Fundamental Flow-Path Design, Optimization and Numerical Analysis of Flow in Axial Turbines

by Heng Hu

LUND
UNIVERSITY

DOCTORAL DISSERTATION
Thesis advisors: Prof. Magnus Genrup, Dr. Narmin Hushmandi.
Faculty opponent: Dr. Cleopatra Cuciumita

To be presented, with the permission of the Faculty of Engineering of Lund University, for public criticism on Friday, the 26th of September at 9:15 AM 2025 in LTH, Lund, Sweden.

Organization
Lund University

Department of Energy Sciences
Box 118
SE–221 00 LUND
Sweden

Document name
DOCTORAL DISSERTATION

Date of disputation
2025-09-26

Sponsoring organisation
China Scholarship Council (CSC)
Energy Sciences Department in Lund

Author(s)
Heng Hu

Title and subtitle
Fundamental Flow-Path Design, Optimization and Numerical Analysis of Flow in Axial Turbines

Abstract

The current study presents a comprehensive research on the design, optimization, and numerical analysis of axial turbines, addressing the immediate need for more efficient and environmentally friendly energy conversion systems. With turbines being central to power generation, aviation, and marine propulsion, enhancing their performance is crucial to reducing fuel consumption, operational costs, and greenhouse gas emissions. The research integrates classical thermodynamic theories with advanced computational methods to create optimized turbine designs capable of meeting modern energy demands.

The study begins with the development of a structured turbine design process, starting from one-dimensional mean-line analysis, progressing through two-dimensional channel design, and culminating in three-dimensional CFD simulations. This multi-step approach ensures a precise evaluation of key performance metrics, such as aerodynamic loading, flow characteristics, and energy conversion efficiency. A significant focus is placed on the impact of blade surface curvature distribution, as even minor modifications can lead to substantial improvements in turbine performance. To explore this, a family of blade curvature distributions is created and analyzed, allowing for the identification of optimal profiles that minimize aerodynamic losses and enhance efficiency. Blade profile optimization is performed using curvature-controlled methods, leveraging Bezier curves to precisely shape blade geometries. The simulations utilize high-fidelity CFD models, while validation against experimental data reinforces the credibility of the findings. Key design cases include the development of a high-pressure partial admission steam turbine and a highly loaded low-reaction low-pressure turbine, both optimized for specific industrial applications. The optimized designs demonstrated improved aerodynamic performance, lower flow separation, and reduced total pressure losses under varying operating conditions. Furthermore, this work extends beyond theoretical studies by applying the optimized designs to real-world scenarios, such as waste heat recovery systems and geared turbofan engines.

In summary, this thesis provides a systematic approach to turbine design and optimization, combining numerical simulation, advanced geometry control, and practical engineering insights. The outcomes offer significant contributions to the fields of energy engineering and turbomachinery, paving the way for the development of high-performance turbines that support the global shift toward more sustainable energy systems.

Key words
Turbine Design, Blade Optimization, Aerodynamic Performance, Surface Curvature

Classification system and/or index terms (if any)

Supplementary bibliographical information

Language
English

ISSN and key title
ISSN:0282-1990
ISRN:LUTMDN/TMHP-25/1184

ISBN
978-91-8104-579-6 (print)
978-91-8104-580-2 (pdf)

Recipient's notes

Number of pages
169

Price

Security classification

Fundamental Flow-Path Design, Optimization and Numerical Analysis of Flow in Axial Turbines

by Heng Hu

LUND
UNIVERSITY

A doctoral thesis at a university in Sweden takes either the form of a single, cohesive research study (monograph) or a summary of research papers (compilation thesis), which the doctoral student has written alone or together with one or several other author(s).

In the latter case, the thesis consists of two parts. An introductory text puts the research work into context and summarizes the main points of the papers. Then, the research publications themselves are reproduced, together with a description of the individual contributions of the authors. The research papers may either have already been published or are manuscripts at various stages (in press, submitted, or in draft).

Funding information: The Chinese Scholarship Council (CSC) and Scholarship from Lund University financially supported the thesis work.

Division of Fluid Mechanics
Department of Energy Sciences
Faculty of Engineering
Box 118
SE 221-00 Lund, Sweden

ISBN: 978-91-8104-579-6 (print)
ISBN: 978-91-8104-580-2 (pdf)
ISSN: 0282-1990
ISRN: LUTMDN/TMHP-25/1184

Printed in Sweden by Lund University, Lund 2025

Every step in the journey of knowledge is a challenge to the old self, an invitation to grow, and a path to becoming something greater.

Contents

List of publications

I **Numerical analysis of an axial high-pressure partial admission turbine**
Heng Hu, Per Askebjer, Magnus Genrup*, Narmin Hushmandi
Turbo Expo: Power for Land, Sea, and Air. American Society of Mechanical Engineers, 2022, 86106: V10BT30A015.
https://doi.org/10.1115/GT2022-81908

II **Numerical investigation on performance of gas turbine blade: effects of simulation models and blade geometry**
Heng Hu, Narmin Hushmandi, Magnus Genrup*
Scandinavian Simulation Society (2023): 184-191.
https://doi.org/10.3384/ecp200024

III **Numerical investigation on performance of a family of curvature distributions of gas turbine blades**
Heng Hu,Narmin Hushmandi, Magnus Genrup*
Manuscript under review for the International Journal of Turbomachinery, Propulsion and Power (IJTPP)

IV **Fundamental flow-path design for geared low-pressure turbines – aspects of cooling**
Heng Hu, Narmin Hushmandi, Magnus Genrup*
Manuscript for submission

Acknowledgements

The completion of my PhD marks the end of a long and meaningful journey. This would not have been possible without the generous support, guidance, and encouragement of many people. It has been both rewarding and challenging, shaped by global events such as the COVID-19 pandemic, personal setbacks, and the relentless pace of research. I am deeply grateful to everyone who made this experience possible and meaningful.

This research was conducted at Lund University's Faculty of Engineering, within the Division of Fluid Mechanics in the Department of Energy Sciences. I sincerely thank the China Scholarship Council (CSC) and the Department of Energy Sciences at Lund University for their generous financial and academic support.

First and foremost, I wish to express my deepest gratitude to my main supervisor, Professor Magnus Genrup, for his unwavering support, patience, and expert guidance throughout my doctoral studies. His insightful feedback and strong belief in my potential helped me grow as a researcher and persevere through many difficult moments. His mentorship has been truly transformative, and I feel privileged to have worked under his supervision.

I am sincerely thankful to Narmin Hushmandi for her valuable guidance, encouragement, and friendship, which supported me through both academic challenges and personal moments. I would also like to thank Mohammad for our many engaging and thought-provoking research discussions, which enriched my work and helped sharpen my ideas. His presence not only made my research smoother and more productive, but also brought joy and laughter to my daily life.

I am grateful to the administrative team at the Department of Energy Sciences, especially Catarina Lindén, Isabelle Frej, Andrea Frydenlund, Sissela Silvmarker, and Anders Schyllert. A very special thank-you goes to Catarina Lindén, whose extraordinary kindness and care accompanied me throughout my PhD journey. I am also deeply thankful to Robert-Zoltán Szász for his unwavering support with software installations and computer-related issues. His prompt responses and patient assistance were always reassuring and much appreciated. My thanks extend to Professor Christer Fureby, Professor Xuesong Bai, Professor Johan Revstedt, Professor Per Tunestål, Docent Hesameddin Fatehi, Docent Rixin Yu, and Marcus Thern for their excellent teaching and support, as well as to Docent Lei Wang and Dr. Himani Garg for their constructive feedback and generous assistance.

To my fellow PhD students and postdocs, including Gustav Karlsson, Arvid Åkerblom, Alexandra Calvén, Francesco Pignatelli, Louise Pierce, Alessandro Ercole, Rasmus Robertsson, Thommie Nilsson, and Morteza Mousavi, Pamella, thank you for the many inspiring conversations, shared experiences, and good times throughout this journey.

To all my colleagues at the department, thank you for the shared laughs, conversations, and daily companionship that lightened the workload. I am especially grateful to my Chinese colleagues over the years, including Yuxiang, Danan, Miao, Yuchen, Xiaoqiao, Miaoxin, Xiufei, Xin Bin, Deiquan, Leilei Xu, Shijie Xu, and many others, for the support and good times that made being far from home feel a little closer to it.

A very special thank-you goes to my boyfriend, Jiazhu, who came into my life at a difficult time and offered endless love, motivation, and strength, enabling me to persevere and complete this PhD. Finally, I owe my deepest gratitude to my parents, Pinchao Hu and Eai Wu, whose unconditional love, unwavering support, and countless sacrifices have laid the foundation for all my achievements. Their encouragement and belief in me have been my greatest source of strength.

Thank you all for being part of this meaningful journey

Popular science summary

Have you ever wondered what powers an airplane or a ship? The answer lies in turbines — machines that convert heat energy into mechanical energy and play a critical role in aviation, marine propulsion, and energy production, as well as in driving industrial processes. While renewable energy sources like wind and solar are gaining popularity, steam and gas turbines remain indispensable for ensuring a stable energy supply. However, with increasing concerns about climate change and rising fuel costs, improving the efficiency and decreasing the environmental impact of these turbines is more important than ever. This thesis focuses on developing new ways to improve turbine performance through advanced design techniques and computer simulations.

Modern turbines are highly complex systems. Even minor design improvements can result in significant fuel savings and lower emissions. One of the key challenges in turbine design is optimizing the shape of the blades—the components responsible for converting high-temperature, high-pressure gas or steam into mechanical power. The shape and curvature of these blades determine how efficiently energy is extracted from the working fluid. This research specifically investigates how different blade surface curvature distributions impact turbine performance and seeks to explore a range of optimal blade shapes that minimize energy loss. To solve this problem, a step-by-step design approach is adopted. It begins with simple, one-dimensional (1D) models to calculate basic parameters like flow rate, energy output, and preliminary stage characteristics. These models are refined into two-dimensional (2D) designs, and subsequently, advanced three-dimensional (3D) computational fluid dynamics (CFD) simulations are used to analyze real-world operating conditions. By using high-fidelity CFD models, this study evaluates a family of blade geometries with varying curvature profiles under different flow conditions and identifies design trends that improve blade efficiency and flow stability. Additionally, grid independence studies and experimental validation ensure that the results are accurate and reliable. Using specialized software, the curvature of turbine blades is precisely designed with Bezier curves, a mathematical tool that ensures smooth flow transitions from the blade inlet to the outlet to achieve optimal aerodynamic performance. This approach allowed for the creation of a "family" of blade designs with varying curvature profiles, each tested to see how it affects blade efficiency and flow stability.

The findings extend beyond theoretical analysis, as the optimized designs

are intended for direct application in industrial practice. For example, the optimized blade designs are used in waste heat recovery systems, which capture and reuse energy that would otherwise be lost. Additionally, the research explores low-pressure turbines for advanced geared turbofan engines, such as those used in aviation, where minimizing cooling requirements and maximizing efficiency are critical for reducing fuel consumption and emissions.

In conclusion, this thesis provides a systematic approach to designing and optimizing turbines, combining engineering principles, computer simulations, and advanced optimization techniques. The results contribute to the development of more efficient and environmentally friendly turbines, helping industries reduce their carbon footprint while maintaining reliable energy production. With continued improvements in turbine technology, we can look forward to a future where energy systems are not only more sustainable but also more cost-effective. Whether it's powering homes, planes, or factories, these advancements bring us one step closer to a cleaner and greener world.

Abstract

The current study presents a comprehensive research on the design, optimization, and numerical analysis of axial turbines, addressing the immediate need for more efficient and environmentally friendly energy conversion systems. With turbines being central to power generation, aviation, and marine propulsion, enhancing their performance is crucial to reducing fuel consumption, operational costs, and greenhouse gas emissions. The research integrates classical thermodynamic theories with advanced computational methods to create optimized turbine designs capable of meeting modern energy demands.

The study begins with the development of a structured turbine design process, starting from one-dimensional mean-line analysis, progressing through two-dimensional channel design, and culminating in three-dimensional CFD simulations. This multi-step approach ensures a precise evaluation of key performance parameters, such as aerodynamic loading, flow characteristics, and energy conversion efficiency. A significant focus is placed on the impact of blade surface curvature distribution, as even minor modifications can lead to substantial improvements in turbine performance. To explore this, a family of blade curvature distributions is created and analyzed, allowing for the identification of optimal profiles that minimize aerodynamic losses and enhance efficiency. Blade profile optimization is performed using curvature-controlled methods, leveraging Bezier curves to precisely shape blade geometries. The simulations utilize high-fidelity CFD models, while validation against experimental data reinforces the credibility of the findings. Key design cases include the development of a high-pressure partial-admission steam turbine and a highly loaded low-reaction low-pressure turbine, both optimized for specific industrial applications. The optimized designs demonstrated improved aerodynamic performance, lower flow separation, and reduced total losses under varying operating conditions. Furthermore, this work extends beyond theoretical studies by applying the optimized designs to real-world scenarios, such as waste heat recovery systems and geared turbofan engines.

In summary, this thesis provides a systematic approach to turbine design and optimization, combining numerical simulation, advanced geometry control, and practical engineering insights. The outcomes offer significant contributions to the fields of energy engineering and turbomachinery, paving the way for the development of high-performance turbines that support the global shift toward more sustainable energy systems.

Nomenclature

Abbreviations

α	Absolute flow angle	C_v	Specific heat at constant volume
β	Relative flow angle; coefficient of volume expansion; acoustic wave angle	N_s	Specific speed
γ	Heat capacity ratio, defined as the ratio of specific heats C_p/C_v	N_{sP}	Power specific speed
Λ	Reaction	W_x	Specific mechanical work
ϕ	Flow coefficient; velocity loss coefficient; cooling effectiveness	Z_w	Zweifel coefficient
ψ	Entropy function; head coefficient; stage loading coefficient	1/2/3D	one/two/three dimensional
ρ	Density	A	Area
τ	Torque	a	Sonic speed; blade section area
v	Blade speed/isentropic expansion velocity ratio	AI	Artificial intelligence
C_0	Isentropic expansion velocity	AM	Additive Manufacturing
C_p	Specific heat at constant pressure	B	Blockage factor
c_p	Pressure coefficient	b	axial chord
C_T	Torque coefficient	B2B	blade-to-blade
C	Absolute velocity; cumulative damage; constant	c	constant
cam	Camberline length	CFD	computational fluid dynamics
D	Diameter	P	Power; power coefficient
DF	Diffusion factor; damage factor	p	Pressure
DNS	Direct Numerical Simulation	Q	Volume flow rate
e	Blade tip clearance; radius of curvature of suction surface between throat and trailing edge	r	Radius
F	Force; fuel-air ratio	RANS	Reynolds-Averaged Navier-Stokes
H	Blade height	Re	Reynolds number
h	Specific enthalpy; convective heat transfer coefficient	RIT	Rotor Relative Inlet Temperature
HP	High pressure	RSM	Reynolds Stress Models
i	Incidence angle	S	Entropy; swirl coefficient; material strength
K	Total pressure loss coefficient; disk cavity core speed ratio; constant	s	Specific entropy; blade spacing; surface distance
L	Length	SOT	Static Operating Temperature
LES	Large Eddy Simulation	SST	Shear-Stress Transport
LP	Low Pressure	T	Temperature
LPTs	low-pressure turbines	t	Blade thickness; time; blade tip to hub section area ratio

m	Mass flow rate; meridional distance	te	Trailing edge thickness
Ma	Mach number	U	Blade speed
N	Rotational speed	u	Specific internal energy
n	Normal direction	v	Specific volume
o	Throat opening	W	Relative velocity
ORC	Organic Rankine Cycles	w	Width
Z	Compressibility factor; blade loading factor; number of blades or vanes	z	Altitude; axial distance

Subscripts and superscript

θ	Tangential	P	Polytropic
0	Total state; zero flow state	p	Profile
1	Stage or stator inlet	PS	Pressure surface
2	Stator exit; rotor inlet	R	Rotor; rupture
3	Stage or rotor exit	r	Radial; referred
f	Friction	ref	Reference
g	Gas	rel	Relative
geo	Geometric	rot	Rotational
h	Hub	S	Stator; secondary flow
i	Ideal; internal	s	Isentropic
in	Inlet	SS	Suction surface
ind	Induced	stg	Stage
int	Internal	T	Turbine
L	Leakage	t	Tip; tangential
LE	Leading edge	TE	Trailing edge
liq	Liquid	th	Throat
m	Meridional; mean; blade metal	ts	Total to static
max	Maximum	tt	Total to total
min	Minimum	u	Yield
n	Normal	w	Windage; wall
x	Axial; extraction point		

Chapter 1

Introduction

1.1 Background

Steam and gas turbines are key technologies in power generation, aviation, and marine propulsion (Figure 1.1). Since the Industrial Revolution, steam turbines have dominated industrial and power generation applications due to their efficient energy conversion capabilities [1]. From the mid-20th century, gas turbines, with their high power density and rapid response, have seen extensive deployment, particularly in aviation [2]. Improving the efficiency of these technologies remains critical for meeting global challenges in climate change and energy sustainability.

Among the various types of turbines, axial turbines are particularly notable for their wide range of applications and high flow capacity in power generation systems [6]. Axial turbines have become the preferred choice for modern gas turbines due to their compact design, high power output, and ability to handle large mass flow rates. These turbines operate by redirecting fluid flow in an axial direction, enabling efficient energy extraction and minimal losses over multiple stages. Their ability to achieve high rotational speeds within a compact volume allows for greater power output and improved energy conversion efficiency, resulting in better equipment. This makes axial turbines essential in both the aviation and power generation industries.

Research into axial turbine design is particularly crucial due to the increasing demand for higher efficiency and lower environmental impact in energy systems. In power generation, axial turbines are essential for achieving

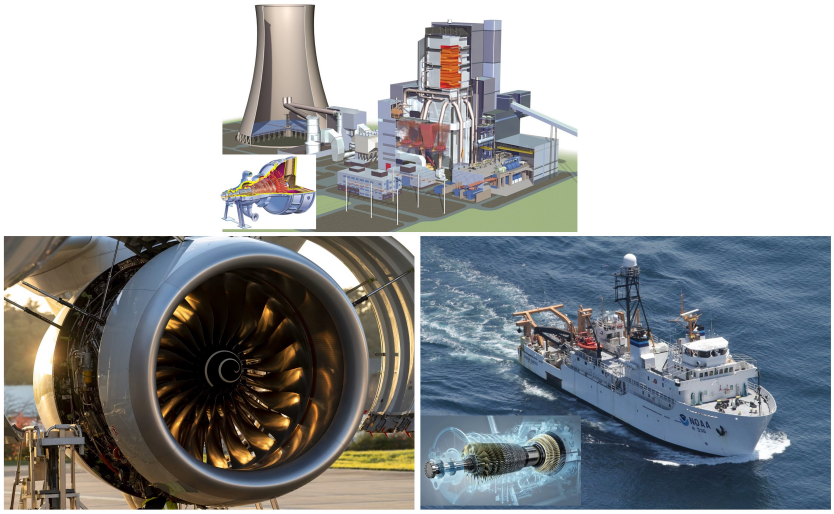

Figure 1.1: Schematic of applications of steam turbines in power plants (top), gas turbine in aerospace (bottom left), and gas turbine in marine propulsion (bottom right). Source: Adapted from GE Power [3], Rolls-Royce [4], and NOAA Marine Operations [5].

high-efficiency combined cycle systems, where their performance directly influences the overall efficiency of the plant. In aviation, axial turbines are at the heart of jet engines, where improving turbine efficiency can significantly reduce fuel consumption and emissions. In addition, the shift towards sustainable energy sources, such as hydrogen and synthetic fuels, requires continuous modifications and improvements in existing axial turbine technology to adapt to new operating conditions [7].

Numerical simulation has become a powerful tool for optimizing turbine designs. It facilitates the analysis of complex fluid dynamics and thermodynamic processes, enabling engineers to test performance virtually and refine designs. By simulating fluid flow, temperature, and pressure distributions, designers can identify and mitigate aerodynamic bottlenecks, ultimately improving efficiency [8]. With the continuous advancement of computational capabilities, accurate numerical modeling is becoming increasingly accessible, thereby improving its applicability in turbine optimization.

Recent technological advancements [9], including additive manufacturing (AM), artificial intelligence (AI), and machine learning [10, 11], have significantly influenced modern turbine design. AM enables the fabrication of intricate geometries, including complex internal cooling channels, which significantly improve thermal management and enhance overall turbine performance [12]. AI-driven optimization techniques have demonstrated

promising improvements in aerodynamic and thermodynamic analysis. Additionally, interdisciplinary approaches that integrate material science with computational methods continue to advance the boundaries of turbine reliability and efficiency [13].

Despite the growing interest in renewable energy sources, conventional fuel-based turbines remain indispensable in various applications. Traditional fuels such as natural gas and coal are supported by mature infrastructure and stable supply, ensuring uninterrupted power output—an attribute that renewable energy has yet to fully match. Gas turbines also offer rapid start-up and strong load-following capabilities, enabling them to respond swiftly to grid demand fluctuations and maintain system stability, particularly under high renewable penetration. Their fuel flexibility allows operation on diverse fuels, including natural gas, synthetic gases, and hydrogen, offering adaptability in the ongoing energy transition. Furthermore, combined cycle power plants, which integrate gas and steam turbines, achieve efficiencies exceeding 60%, and their proven economic viability and technological maturity sustain their dominance in large-scale power generation. In addition, conventional fuel-driven turbines remain widely used across industrial and transportation sectors, supported by well-established maintenance and operational systems. These advantages ensure their continued relevance for the foreseeable future [14]. Concurrently, ongoing research and development in low-carbon fuel technologies, such as hydrogen and synthetic fuels, present new opportunities to transform traditional turbine systems into more environmentally sustainable and efficient configurations [15].

The current thesis adopts a best-practice design methodology to optimize the final turbine configuration using advanced blade profiling techniques and evaluates the optimized cases with advanced numerical simulation. The primary aim is to improve aerodynamic performance and reduce energy losses, contributing to the development of high-efficiency, low-emission energy conversion systems.

1.2 State-of-Art literature review

1.2.1 Design of axial gas turbines

In recent years, the design of axial-flow gas turbines has faced growing challenges. Traditionally, turbine design has focused on maximizing aerodynamic efficiency at a fixed design point, following a relatively stable,

single-point optimization approach. However, with more diverse operating conditions and rapid technological progress [16], this design philosophy is gradually shifting toward a more comprehensive and adaptable strategy. Increasing demands for higher blade loading, wider operating ranges, stricter emission regulations, and the integration of advanced manufacturing methods such as additive manufacturing are reshaping the landscape of turbine design.

One of the main trends is the push towards highly loaded gas turbine stages to achieve greater energy extraction within compact architectures. A highly loaded turbine refers to a design in which greater energy conversion is achieved within a shorter and more compact blade passage [17]. It represents a key direction in the development of a higher thrust-to-weight ratio and improved performance. Studies such as those by Rezaienia et al. [18] and Ainsworth et al. [19] demonstrate that while higher loading increases the energy extracted per stage, it also intensifies flow separation risks, boundary layer thickening, and shock-induced losses, particularly near the suction surfaces and endwalls. Yue Li et al. [20] introduced a compact design into the first-stage blade of the highly loaded turbine, which effectively reduced aerodynamic losses near the endwall region, with mechanisms clarified through numerical analysis. Bouterra S et al. [21] investigate the flow separation behavior, with a focus on the impact of slat configurations. The instantaneous velocity field iso-surfaces (as shown in Figure 1.2) depict flow separation on the suction surface and trailing edge, characterized by low-speed regions and vortical structures.

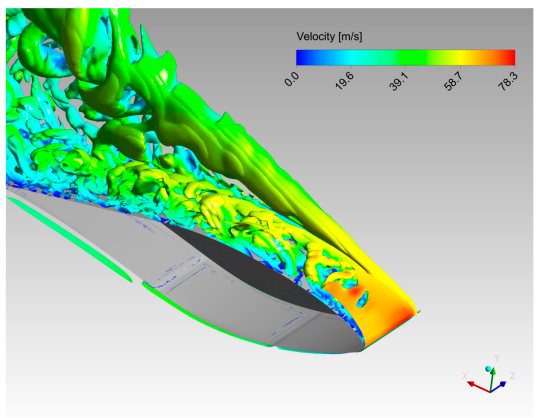

Figure 1.2: Iso-surfaces colored by velocity, showing flow separation near the suction surface and trailing edge [21].

Simultaneously, the interaction between adjacent stator-stator or rotor-rotor rows is one of the key factors contributing to variations in unsteady

aerodynamic loads within a turbine, due to changes in flow features such as potential flow, wake, and secondary flow structures [22]. Three-dimensional aerodynamic design has gained prominence. Techniques such as endwall contouring, leaning, and sweeping of blades are increasingly employed to control secondary flows and suppress loss generation mechanisms. As reported by Lardeau et al. [23] and Zhang et al. [24], optimized 3D blade shaping can significantly reduce endwall losses, enhance flow uniformity, and improve off-design performance.

Another critical development is the utilization of advanced materials and additive manufacturing technologies. The freedom offered by AM enables the creation of complex blade features, such as integrated cooling passages and intricate surface curvature variations, which were previously infeasible with traditional manufacturing methods. Research by Martinez et al. [25] and Huang et al. [26] highlights how these innovations allow designers to push aerodynamic optimization further, balancing aerodynamic performance with mechanical and thermal robustness.

Moreover, modern gas turbine designs increasingly emphasize robustness across a wide operating range. With operational scenarios involving frequent load changes, partial load operations, and transient conditions, it is no longer sufficient to optimize solely for peak performance at a single design point. Instead, as outlined by Lee and Gielski [27], turbines must maintain acceptable aerodynamic performance across a broad range of incidence angles and Mach numbers. This trend necessitates novel design approaches that prioritize flow stability, stall margin enhancement, and robustness to variations in operating points and boundary conditions.

Despite these advancements, several persistent challenges remain. Achieving optimal trade-offs between high efficiency, wide-range stability, and manufacturability continues to be challenging. Particularly, flow phenomena such as shock-boundary layer interactions, flow separations near suction peaks, and three-dimensional secondary flows pose significant obstacles to realizing the full benefits of advanced blade shaping and high-load operation. Thus, a fundamental and systematic investigation into axial gas turbine flow-path design, blade surface optimization [28], and numerical analysis becomes essential. A deeper understanding of the coupled influence of blade curvature distribution, incidence variation, and three-dimensional flow structures is necessary to push the current design boundaries further.

1.2.2 Design of axial steam turbines

Axial steam turbines remain a critical component in modern energy systems, particularly in applications involving heat recovery and sustainable power generation. With increasing attention to energy efficiency and carbon neutrality, the Organic Rankine Cycle (ORC) [29–31] has emerged as a promising technology for converting low-grade heat, such as industrial waste heat or geothermal energy into useful power. Due to their compact size and suitability for low to medium power outputs, axial steam turbines are frequently employed as expanders in ORC systems. Nazari et al. [32] proposed a waste heat recovery system that integrates a subcritical steam Rankine cycle with a transcritical organic Rankine cycle, specifically designed for a combined steam ORC application.

Previous studies have extensively investigated compact, high-pressure supersonic turbine designs. Seume et al. [33] provided valuable insights into aerodynamic and thermodynamic design as well as testing of supersonic turbines within small-scale ORC applications. Paniagua et al. [34] demonstrated the potential of entropy-minimization strategies and oblique shock wave usage to significantly reduce aerodynamic losses. Rashid et al. [35] further highlighted the complexity of supersonic flow interactions within Curtis stages, emphasizing the need for detailed flow field analyses. In addition, Ghio et al. [36] revealed discrepancies between numerical predictions and experimental data for supersonic impulse turbine stages, attributing these differences primarily to numerical diffusion and measurement probe interference in high-gradient supersonic regions.

In such small-scale steam turbine applications, partial-arc admission is often adopted to accommodate variable operating loads and reduce mechanical complexity. However, this configuration introduces unique aerodynamic challenges, including strong shock-wave interactions, non-uniform flow fields, and unsteady aerodynamic forces acting on the rotor blades. These phenomena can significantly affect the performance and mechanical reliability of the turbine. According to Fridh et al. [37], turbines with single-blocked arc admission demonstrate superior aerodynamic performance compared to multiple arc-blocked designs due to minimized filling and emptying losses. Nonetheless, unsteady phenomena arising from partial arc admission, including significant shock wave interactions, still require comprehensive analysis and optimization to further improve efficiency and reliability.

1.2.3 Blade geometry and curvature optimization

The efficiency of aeroengines depends on key components such as the combustor, compressor, and turbine, and improvements to any of these components enhance overall performance. In turbines, aerodynamic loss is a major factor limiting efficiency, resulting from irreversible energy dissipation in the blade passages. Among its causes, blade geometry, particularly the spanwise distribution of surface curvature, plays a central role in determining aerodynamic behavior. Strategic modulation of blade curvature across spanwise sections enables control over critical aerodynamic parameters, including pressure gradient distribution, boundary-layer evolution, and flow separation, all of which are closely associated with profile losses. These considerations have motivated extensive research into curvature-based blade design strategies in recent years.

Early turbine blade design practices typically focused on discrete geometric parameters such as camber, thickness distribution, and leading and trailing edge shapes. However, research by Shen et al. [38] and Song et al. [39] demonstrated that ensuring continuous and smoothly varying curvature distributions leads to better boundary layer stability and suppresses separation bubbles, especially under high-loading conditions. In addition to mid-chord curvature control, Hamakhan et al. [40] emphasized that smooth curvature transitions at the leading edge are critical to avoiding flow disturbances. The suppression of flow separation has long been recognized as a key factor in improving blade performance [41], and the distribution of surface curvature strongly influences both separation and aerodynamic loading [42]. Elewe [43] further demonstrated through numerical simulations how variations in curvature impact airfoil performance.

Advances in parametric modeling have enabled more refined control of blade curvature. The use of Bézier curves and other surface-fitting techniques allows precise manipulation of local curvature while maintaining geometric smoothness. Korakianitis et al. [44] proposed the CIRCLE method, which prescribes curvature distributions to optimize aerodynamic performance while ensuring manufacturability. More recently, machine learning and optimization algorithms have further expanded design capabilities: Guo et al. [45] and Wu et al. [46] integrated artificial intelligence into curvature optimization processes, discovering non-intuitive yet highly efficient blade shapes that surpass traditional designs. Furthermore, the interaction between blade curvature and secondary flows has attracted increasing attention. Park et al. [47] showed that careful curvature design can mitigate

secondary flow losses, particularly near endwalls where flow separation and cross-passage pressure gradients dominate.

1.2.4 Numerical simulations and optimization

Numerical simulation has become an indispensable tool in the design and analysis of axial turbine flow paths. With the increasing complexity of turbine geometries and operating conditions, CFD provides critical insights into flow structures, loss mechanisms, and unsteady aerodynamic behavior that are often difficult to capture with 1D and 2D design methodologies.

RANS simulations remain the primary method for industrial turbine flow simulations due to their balance between accuracy and computational cost. Recent improvements in turbulence modeling, particularly with the SST k-ω model, have enhanced the reliability of RANS for predicting boundary layer separation and shock interactions. Studies such as those by Sandberg et al. [48] and Fu et al. [49] have validated the capabilities and limitations of RANS methods in capturing key aerodynamic features of turbine cascades.

However, the increasing need for higher fidelity predictions, especially in high-loaded and highly three-dimensional flow conditions, has motivated the adoption of hybrid RANS-LES approaches. Research by Michelassi et al. [50] and Bogojevic et al. [51] demonstrated that scale-resolving simulations provide more accurate predictions of loss generation mechanisms, vortex structures, and unsteady flow features, although at significantly higher computational costs. In addition to turbulence modeling advances, grid generation techniques have evolved to better resolve critical flow regions such as shock waves, separation bubbles, and secondary flows. Zhang et al. [52] highlighted the importance of anisotropic meshing strategies in improving solution accuracy without excessive mesh growth. Meanwhile, time-accurate simulations have been increasingly utilized to capture unsteady phenomena such as rotating stall, wake-blade interactions, and vortex shedding, as shown by Hillewaert et al. [53]. Moreover, the integration of optimization algorithms with CFD has expanded the role of numerical simulations from passive analysis to active design tools. Recent work by Zhao et al. [54] combined adjoint-based optimization with unsteady CFD simulations to achieve significant aerodynamic performance improvements in high-pressure turbines.

Accurately predicting shock-boundary layer interactions, low Reynolds number transitional effects, and condensation phenomena under wet steam

conditions still pose difficulties. Furthermore, the computational expense of high-fidelity simulations restricts their widespread application in full-annual or multi-stage turbine configurations. Therefore, a careful balance between modeling fidelity, computational feasibility, and physical relevance must be maintained. This dissertation addresses these issues by employing validated numerical methods to analyze turbine flow features, optimize blade profiles, and systematically investigate the interactions between flow structures, blade geometry, and operating conditions in axial turbines.

1.3 Motivation

Although current research trends have increasingly shifted toward replacing conventional fuels with more environmentally friendly alternatives, a complete transition will still take decades to accomplish. Therefore, continuous enhancement of existing technologies remains essential for achieving more efficient and sustainable operations during this transitional period. For example, improving the efficiency of a typical aircraft engine by just one percent can reduce carbon dioxide emissions by several hundred tons annually. Therefore, my research aims to further improve turbine efficiency and performance through design and optimization, reduce emissions, and address the limitations of existing technologies.

- Potential for improvements in existing turbine technology: Although traditional turbine engine technology is highly mature, there remains considerable potential for improvement in terms of efficiency enhancement and emission reduction, particularly to meet the demands of the modern energy transition.
- Immaturity of alternative technologies: Despite rapid advancements in new propulsion technologies such as fuel cells and electric propulsion, these alternatives are not yet fully capable of replacing traditional turbine engines in high-power and heavy-load applications. Therefore, further optimization of traditional turbine designs remains a practical necessity.
- Meeting transitional demands of future energy structures: Until a complete shift to renewable energy is realized, traditional turbine engines will continue to play a vital role. Hence, optimizing and improving their performance is an essential step in the ongoing emission-reduction process.

1.4 Objectives

The primary objective of this research is to develop efficient designs for axial turbines that meet specific performance requirements through a comprehensive and systematic design methodology. This is achieved by integrating aerodynamic optimization and numerical simulation across the full design process. Specifically, the key objectives of this study include:

- Apply a complete axial turbine design workflow, from mean-line 1D analysis to full-annulus 3D CFD simulations, enabling precise evaluation and enhancement of aerodynamic performance in a conventional turbine.
- Optimize blade geometry and curvature using advanced parameterization techniques (e.g., Bezier curves), targeting efficiency improvements and emission reductions in line with modern energy-transition requirements.
- Investigate the aerodynamic behavior of various geometric configurations and operating conditions for high-power, heavy-load applications where alternative propulsion technologies remain immature, proposing targeted design refinements to minimize losses and improve overall efficiency
- Assess turbine performance under transitional energy scenarios, ensuring that optimized designs maintain high efficiency and operational reliability until full renewable-energy adoption is achieved.

This thesis aims to contribute to the field of axial turbine design technology by providing a systematic approach to numerical optimization of aerodynamic performance. The findings are expected to benefit both traditional and emerging turbine technologies, supporting the development of more efficient and sustainable energy conversion systems.

1.5 Thesis outline and scope

The research presented in this thesis focuses on the design, aerodynamic optimization, and numerical analysis of axial turbines, with particular emphasis on improving efficiency, and adaptability for next-generation energy

systems. Figure 1.3 illustrates the turbine design and optimization workflow, starting from mean-line analysis, progressing through through-flow design, airfoil geometry generation, and 2D/3D aerodynamic analysis, with iterative feedback between stages to refine the design.

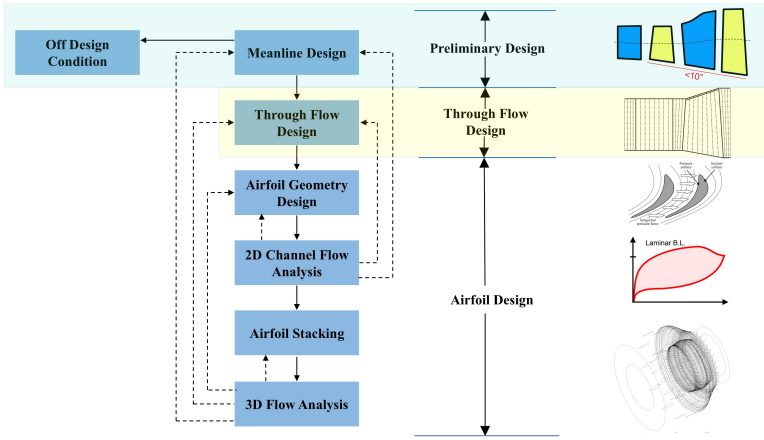

Figure 1.3: Workflow of the integrated axial turbine design framework, from preliminary mean-line analysis to final three-dimensional CFD validation.

The design and optimization methodologies are applied to two major industrial applications in this thesis: axial steam turbines and axial gas turbines. The first case addresses the development of a compact supersonic steam turbine operating in a partial-admission configuration, aimed at satisfying the specified working conditions of the Heat Recovery Cascade System. Due to the compact layout and specific operating conditions, strong shock waves inevitably arise within the flow field. A central focus of this part of the study is the proper management of shock waves and the mitigation of unsteady aerodynamic forces induced by partial admission and shock wave interactions, to ensure mechanical reliability and performance stability. In the second application, the research targets low-pressure turbines (LPTs) used in future-generation turbofan engines. The focus is on enhancing aerodynamic efficiency by optimizing blade profiles through curvature-controlled design, evaluating surface pressure diffusion, and managing Mach number distribution. Furthermore, three-dimensional CFD simulations are conducted to capture complex flow phenomena such as shock wave interactions and spanwise pressure gradients, providing critical insights into aerodynamic behavior. Such a comprehensive analysis allows for an accurate assessment of blade performance and the implementation of advanced aerodynamic features across the full turbine design process.

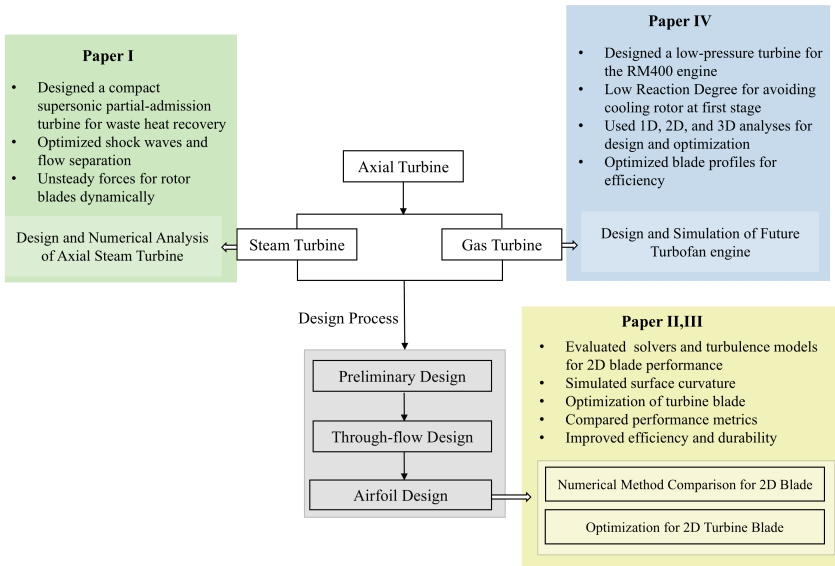

Figure 1.4: Scope and structure of the present research, based on four key papers (Paper I–IV), showing the main study areas and their interrelation within the overall turbine design framework.

The research framework is structured around four key papers, as illustrated in Figure 1.4, which outlines the design process and application domains of axial turbines, including both steam and gas turbines. Paper I explores the design and numerical analysis of axial steam turbines, addressing challenges such as flow separation and dynamic forces in a partial-admission turbine. Papers II and III evaluate numerical solvers and turbulence models for 2D blade optimization, investigating surface curvature effects and improving aerodynamic performance. Paper IV examines first-stage low-reaction high loading turbine designs for the RM400 turbofan engine, emphasizing rotor cooling reduction and efficiency improvement. Across all papers, numerical tools and optimization techniques, including design parameterization and CFD simulations, are employed to further refine the design and adaptability of modern turbines to meet the needs of better operational compatibility.

Chapter 2

Preliminary and through-flow design

This chapter provides the fundamental principles of the design and analysis of axial turbines. This process involves several key steps, beginning with the initial design specifications and concluding with the detail design of the flow passages [55–59]. The focus of this chapter is the design and selection of the primary geometric parameters that define the overall configuration of the blade row—an essential foundation for the subsequent profiling of the blade itself, which will be addressed in the next chapter.

2.1 Basic principles

2.1.1 Fundamental principles of flow expansion

To understand the governing parameters of turbine performance, it is essential to first analyze the mechanism of energy extraction from the working fluid. The expansion process in turbines involves the efficient conversion of a fluid's thermal and kinetic energy into mechanical work. The fluid velocity can be composed into three different components, the tangential velocity component C_θ, the axial velocity component C_x and the radial velocity component C_r, as shown in Figure 2.1. The axial velocity component primarily determines the mass flow rate, while radial components are generally small in axial turbines and mainly associated with secondary flows that can influence axial force. However, neither of these components

directly contributes to the energy exchange. The actual energy exchange occurs through changes in the tangential velocity component, as expressed by Euler's turbomachinery, detailed as follow [60].

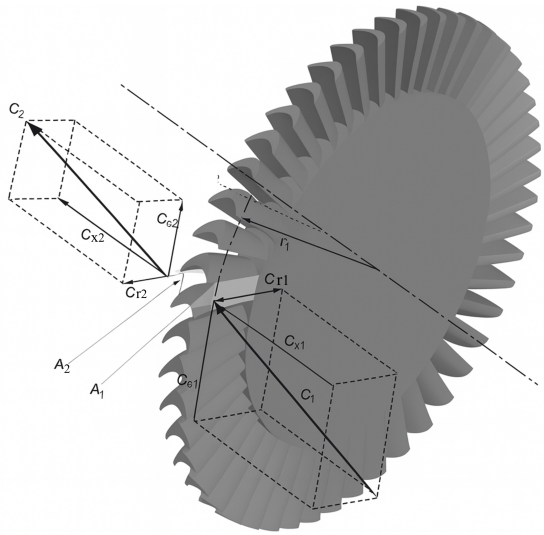

Figure 2.1: Schematic of a turbine blade row illustrating the decomposition of the absolute fluid velocity $\mathbf{C}$ into axial C_x (parallel to the shaft), radial C_r (normal to both shaft and circumference), and tangential C_θ (perpendicular to the radius) components [60].

According to Newton's second law of motion in the angular frame of reference, the torque developed is equal to the rate of angular momentum across any blade row:

$$\tau = \dot{m}(r_2 C_{\theta 2} - r_1 C_{\theta 1}), \tag{2.1}$$

where $\dot{m}$ is the mass flow rate, r the radius, and C_θ the tangential velocity component. Consequently, the power output can be further defined as:

$$P = \tau\omega = \dot{m}(U_2 C_{\theta 2} - U_1 C_{\theta 1}), \tag{2.2}$$

where ω is the angular speed of the rotor and the blade speed is given by $U = \omega r$. Thus, at the mean radius, the specific work (work output per unit mass flow), known as the Euler turbomachinery equation [61], is defined as:

$$w = U_2 C_{\theta 2} - U_1 C_{\theta 1}. \tag{2.3}$$

This equation applies to all types of turbomachinery. Its application to axial turbines can be illustrated using the velocity triangles and Mollier diagram. If we consider the particular case of an axial turbine, the flow enters the stage at state 1, expands through the stator to state 2, and through

the rotor to state 3. Figure 2.2 shows a typical single-stage turbine expansion process on a Mollier enthalpy-entropy diagram along with the velocity triangles. The Mollier diagram provides a thermodynamic representation between enthalpy (h) and entropy (s) at various states, illustrating both total and static properties, as well as actual and ideal isentropic expansion processes. Under ideal adiabatic conditions without coolant flow and neglecting viscous losses, the total enthalpy remains constant across the stator, whereas it decreases across the rotor blades where mechanical work is extracted.

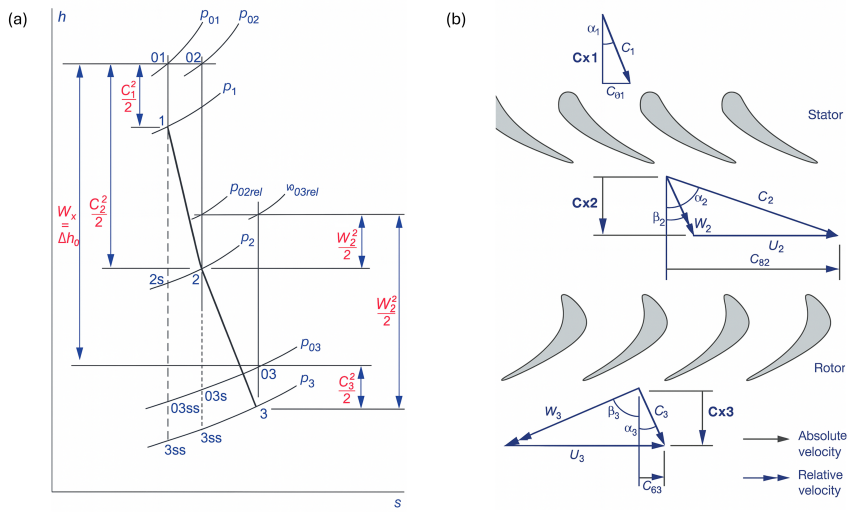

Figure 2.2: (a) Mollier enthalpy-entropy diagram, (b) Velocity vectors over a stage. (Adapted from Moustapha, 2021 [62]).

Thermodynamically, the total work output extracted per unit mass, i.e. specific work, across the stage is calculated from Equation 2.4:

$$w = h_{01} - h_{03}. \tag{2.4}$$

where h_{01} and h_{03} denote the total (stagnation) enthalpy at the stage inlet and outlet, respectively.

Another important concept in turbomachinery property is rothalpy, which provides a conserved property along a rotor passage under steady, adiabatic conditions without body forces. Rothalpy, I, is defined as:

$$I = h_{0,\text{rel}} - \frac{1}{2}U^2 = Constant. \tag{2.5}$$

where $h_{0,\text{rel}}$ is the relative stagnation enthalpy defined by eq:relenthalpy and U is the local blade speed. The relative stagnation enthalpy is given by:

$$h_{0,\text{rel}} = h + \frac{W^2}{2}. \tag{2.6}$$

where h is the static enthalpy and W is the relative velocity (velocity of the fluid to the rotating blade). In the absence of body forces and heat transfer, rothalpy is conserved through the rotor:

$$h_2 - h_3 = \frac{1}{2}(U_2^2 - U_3^2) - \frac{1}{2}(W_2^2 - W_3^2). \tag{2.7}$$

By combining the principles of energy conservation and the invariance of rothalpy, the specific work done by the rotor stage can be further expressed as:

$$w = \frac{1}{2}\Big[(U_2^2 - U_3^2) - (W_2^2 - W_3^2) + (C_2^2 - C_3^2)\Big]. \tag{2.8}$$

where C denotes the absolute velocity.

Under the condition of constant mean radius (i.e., $U_2 = U_3$), which is a reasonable assumption for many axial turbine stages, this equation simplifies to:

$$w = \frac{1}{2}\Big[(W_3^2 - W_2^2) + (C_2^2 - C_3^2)\Big]. \tag{2.9}$$

From Equation 2.9, the physical interpretation is as follows. To produce positive work, the relative velocity must increase through the rotor (that is, $W_3 > W_2$), signifying expansion of the relative flow within the rotor. Meanwhile, the decrease in absolute velocity ($C_2 > C_3$) indicates the transfer of work within the rotor. The velocity C_2 is the result of the acceleration of the working fluid in the stator of the turbine, and highlights the importance and purpose of this component. The velocity C_3 is the result of the combination of the vectors of the relative velocity leaving the rotor and the local blade speed, and if these vectors are similar in magnitude and opposed in direction, the resulting value of C_3 will be lower than either. Theoretically, these relationships represent the fundamental mechanisms of energy transfer in a turbine stage. The conservation of total enthalpy throughout the stage confirms that the extracted work results solely from the expansion of the fluid.

2.1.2 Turbine parameters

Turbine stage performance and design are fundamentally characterized by a set of non-dimensional parameters, which enable the systematic comparison and optimization of different configurations across a wide range of operating conditions. These key parameters include various definitions of efficiency, the stage loading coefficient, the flow coefficient, and the degree of reaction, among others. Their judicious selection and interrelationship dictate the fundamental operating characteristics and achievable performance of axial turbines [63, 64].

2.1.2.1 Turbine efficiency

The thermodynamic efficiency of a turbine is defined as the ratio of the actual change in energy to the ideal change in energy [65]. If the ideal work is taken as that of an isentropic process, the total-to-total isentropic efficiency (η_{tt}) quantifies the ratio of the actual work output to the ideal (isentropic) work output for expansion between the total conditions at the turbine inlet and outlet:

$$\eta_{tt} = \frac{h_{01} - h_{03}}{h_{01} - h_{03s}}. \tag{2.10}$$

where h_{03s} is the total enthalpy at the outlet corresponding to an ideal isentropic process. This definition assumes an adiabatic process and is often used in gas turbines where the kinetic energy at the outlet is recoverable.

The total-to-static efficiency (η_{ts}) compares the actual work output to the ideal work output referenced to the total inlet and static outlet conditions:

$$\eta_{ts} = \frac{h_{01} - h_3}{h_{01} - h_{3s}}. \tag{2.11}$$

where h_3 is the static enthalpy at the outlet and h_{3s} is the corresponding isentropic value. The choice between η_{tt} and η_{ts} depends on the application and the stage within a multi-stage arrangement, but both provide critical insight into the thermodynamic quality of the expansion process.

2.1.2.2 Flow coefficient

The flow coefficient (ϕ) is defined as the ratio of axial velocity to blade speed [65]:

$$\phi = \frac{C_x}{U}. \tag{2.12}$$

The flow coefficient characterizes the relative magnitude of throughflow velocity compared to the blade's rotational motion, directly influencing stage mass flow rate, passage area, and velocity triangles. The flow coefficient governs the overall stage diameter, as it is related to the annulus area A. A low ϕ results in a larger annulus and longer blades, which in turn increases centrifugal stress. If the priority is to minimize blade stress, stage size, or weight, a higher flow coefficient should be selected. Furthermore, ϕ is closely related to the specific speed (N_s) and specific diameter (D_s), providing an additional link between aerodynamic design parameters and turbomachinery similarity criteria [65].

2.1.2.3 Stage loading coefficient

The stage loading coefficient (ψ) is a dimensionless parameter that expresses the specific work output of a turbine stage normalized by the square of the rotor blade speed. For compressible flows, it is defined as [65]:

$$\psi = \frac{\Delta h_0}{U^2}. \tag{2.13}$$

Alternatively, considering the definition of total enthalpy for a stage, stage loading can be expressed in terms of the flow coefficient (ϕ) and the absolute flow angles at the rotor inlet and outlet (α_2 and α_3):

$$\psi = \phi(\tan\alpha_2 - \tan\alpha_3). \tag{2.14}$$

where the absolute flow angles α_2 and α_3 are related to the relative angles β_2 and β_3 by:

$$\tan\alpha_2 = \tan\beta_2 + \frac{1}{\phi}, \tag{2.15}$$

$$\tan\alpha_3 = \tan\beta_3 + \frac{1}{\phi}. \tag{2.16}$$

Therefore,

$$\psi = \phi(\tan\beta_2 - \tan\beta_3). \tag{2.17}$$

The loading coefficient governs the degree of energy extraction per stage, with higher values indicating increased work per unit mass flow. In preliminary design, ψ serves as a principal parameter for scaling turbine performance and is directly linked to the turning angle of the flow within the blade passages.

As the loading coefficient ψ increases, greater flow turning is required within the blade passages (i.e., larger changes in relative flow angle, $\beta_2 - \beta_3$). This increased turning elevates surface area exposure to the working fluid, intensifying boundary layer development and secondary flow generation, both of which contribute to aerodynamic losses. High loading stages, therefore, tend to experience greater profile losses due to higher surface friction and more pronounced secondary flow structures.

Conversely, a low loading coefficient means less work per stage, requiring more stages to meet the total work output, which increases turbine complexity, weight, and cost, and may raise cumulative losses that reduce overall efficiency. Given power and mass flow constraints, lowering ψ to improve efficiency often demands higher blade speed, thereby increasing blade stresses and posing mechanical challenges.

The Smith chart [66] is a classical tool in axial turbine preliminary design that illustrates the relationship between two key nondimensional parameters, the flow coefficient ϕ and the stage loading coefficient ψ, and their combined influence on aerodynamic performance. Although not intended for precise performance prediction, the chart (Figure 2.3) effectively indicates efficiency trends by mapping contours of constant efficiency over the typical operating ranges of ϕ and ψ, thereby showing regions of near-optimal aerodynamic performance.

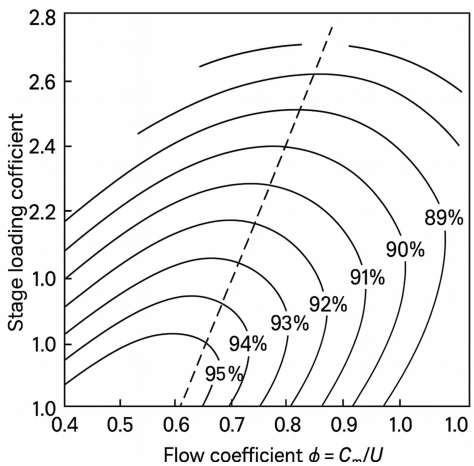

Figure 2.3: Smith chart of turbine stage efficiency [66].

The Smith chart is often the starting point for selecting preliminary ϕ and ψ values, providing a framework for design trade-offs that balances aerodynamic performance with mechanical and operational constraints. It also

helps define feasible operating envelopes and guide the scaling of turbine stages to achieve targeted performance goals.

2.1.2.4 Degree of reaction

The degree of reaction (Λ) is defined as the fraction of the static enthalpy drop that occurs in the rotor as opposed to the total static drop that occurs in the stage [65], serving as a critical determinant of the velocity distribution, pressure gradients, and blade loading:

$$\Lambda = \frac{h_2 - h_3}{h_1 - h_3}. \tag{2.18}$$

where $h_1 - h_3$ represents the total static stage enthalpy drop in the stage. In the repeating stages where $\vec{C_1} = \vec{C_3}$, then $h_1 - h_3$ can be written as $h_{01} - h_{03}$ (often parameterized as ψU^2), and $h_2 - h_3$ is the static enthalpy change across the rotor, which can be related to velocity components as:

$$h_2 - h_3 = \frac{w_3^2 - w_2^2}{2} = \frac{C_x^2}{2}(\tan^2 \beta_3 - \tan^2 \beta_2). \tag{2.19}$$

Thus:

$$\Lambda = \frac{\phi^2}{2\psi}(\tan^2 \beta_3 - \tan^2 \beta_2). \tag{2.20}$$

where h_1 and h_2 represent static enthalpy at rotor inlet and outlet respectively, and h_3 is static enthalpy at stage exit. These expressions assume constant axial velocity across the stage. Reaction governs the distribution of expansion between stator and rotor, thereby dictating the velocity triangles, blade shapes, and operational characteristics.

A systematic variation of reaction has significant implications for stage aerodynamics and loss mechanisms: Small positive reaction: Requires the stator to deliver high flow velocities to the rotor, increasing the potential for frictional losses, supersonic flow, and shock formation. Careful aerodynamic design is necessary to manage these effects. Medium (balanced) reaction: yields a distribution of expansion between stator and rotor, lowering velocity extremes and turning angles, and generally optimizing stage efficiency. This regime supports moderate blade loading and mitigates loss sources. High reaction: the majority of the enthalpy drop occurs in the rotor, resulting in higher velocities and blade loadings within the rotor. This condition can exacerbate three-dimensional flow effects, increase frictional

and tip-leakage losses, and impose additional constraints on mechanical design due to elevated rotational speeds and associated blade stresses.

To further investigate the practical impact of reaction on turbine thermal performance, particularly on the thermal load experienced by the rotor, Paper IV implements a very low reaction in the first-stage rotor. This design aims to reduce the rotor relative inlet temperature ($\mathrm{RIT_{rel}}$) and thereby eliminate the need for active rotor cooling. Since $\mathrm{RIT_{rel}}$ is a key indicator of thermodynamic performance in turbines, the analytical derivation is presented below.

The total (stagnation) temperature in the absolute and relative frames for a perfect gas are defined as [67, 68]:

$$T_0 = T + \frac{C^2}{2\,c_p}, \tag{2.21}$$

$$T_{0,\mathrm{rel}} = T + \frac{W^2}{2\,c_p}. \tag{2.22}$$

where c_p is specific heat at constant pressure, T_0 is the stagnation temperature and T is the static temperature. Since there is no work extraction in the stator and the process is adiabatic, the total temperature at the stator inlet equals the stator exit total temperature (SOT), assuming no losses. $T_{0,\mathrm{rel}}$ is the rotor relative inlet temperature ($\mathrm{RIT_{rel}}$).

Subtracting the two definitions gives the relative $\mathrm{RIT_{rel}}$:

$$\mathrm{RIT_{rel}} = \mathrm{SOT} + \frac{W^2 - C^2}{2\,c_p}. \tag{2.23}$$

By applying the fundamental fluid motion equations, Euler's turbomachinery work relation, and the definition of stage reaction, one can derive the following expressions:

$$\mathrm{RIT_{rel}} = \mathrm{SOT} - \frac{\Delta T_0}{2} - \frac{U^2}{2\,c_p}\,(1 - 2\,\Lambda), \tag{2.24}$$

where ΔT_0 is the total temperature drop, non-dimensionalized via the relation $\Delta h_0 = \Delta T_0 c_p$,

$$\frac{\mathrm{SOT} - \mathrm{RIT_{rel}}}{\Delta T_0} = \frac{1}{2} - \frac{1}{\psi}\Big(\Lambda - \tfrac{1}{2}\Big). \tag{2.25}$$

As Λ decreases, more of the static enthalpy drop occurs in the stator, thus increasing the temperature drop across the stator. This results in a lower

RIT, thereby diminishing the thermal loading on the rotor blades and mitigating the need for active blade cooling measures. In practical applications, lowering the first-stage reaction reduces the $\mathrm{RIT}_{\mathrm{rel}}$. By eliminating the complexities and costs associated with rotor cooling systems, this approach can enhance component durability and overall turbine performance.

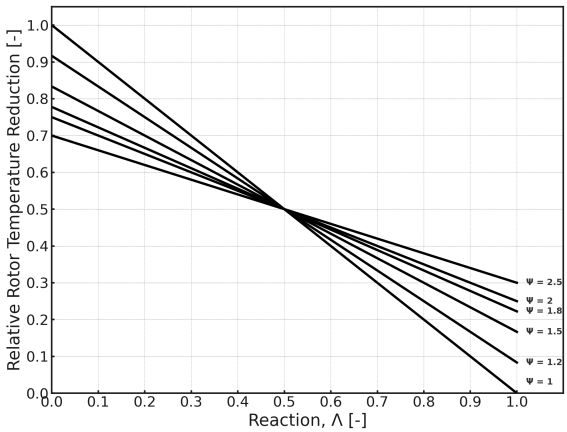

Figure 2.4: Normalized rotor temperature reduction $(\mathrm{SOT} - \mathrm{RIT}_{\mathrm{rel}})/\Delta T_0$ versus stage reaction Λ, for various loading coefficients ψ.

Figure 2.4 plots the normalized rotor temperature reduction as a function of stage reaction Λ for various loading coefficients ψ, based on the analytical equation 2.25. All straight lines radiate from the common intersection at $\Lambda = 0.5$, where the relative inlet temperature rise is exactly half the total temperature rise. For $\Lambda < 0.5$, more of the enthalpy drop occurs in the stator, so the normalized reduction—and thus the decrease in $\mathrm{RIT}_{\mathrm{rel}}$—grows as the reaction is reduced.

2.1.2.5 Incidence and deviation

Incidence refers to the angle difference between the flow angle and the blade inlet metal angle [69]. It comprises two principal components:

(a) Design (induced) incidence: Even under nominal design conditions, blade loading caused by the turning of streamlines upstream of and at the inlet to the blade passage gives rise to a small positive incidence, which induces a minor flow deflection toward the pressure side at the leading edge. For reaction-type blades, the induced incidence typically ranges from 2° to 4° [70].

(b) Off-design incidence: When operating conditions deviate from the design point, the incidence angle can vary significantly. Excessive positive incidence causes over-acceleration and thickening of the suction surface boundary layer, increasing the risk of flow separation and loss generation. Negative incidence is usually better tolerated until a critical negative stalling limit is reached, beyond which performance deteriorates rapidly [65].

Deviation quantifies the difference between the geometric blade exit angle and the actual flow exit angle, resulting from a combination of blade loading and geometric effects. Deviation arises from both two-dimensional effects, such as non-uniform pressure gradients and streamline curvature between suction and pressure surfaces, and 3D effects, including secondary flows, radial migration, tip leakage, and endwall boundary layer interactions. These mechanisms combine to cause streamline deflection near the trailing edge, manifesting as exit flow deviation, which in turn directly impacts stage performance and aerodynamic loss characteristics. Deviation is typically estimated via empirical correlations during preliminary design.

2.1.2.6 Flow capacity

Flow capacity characterizes the normalized mass flow admitted by the turbine, accounting for prevailing total temperature and pressure conditions [71]. This parameter enables consistent comparison of mass flow capabilities across diverse operating regimes and is defined as:

$$\text{Flow Capacity} = \frac{\dot{m}\sqrt{T_0}}{p_0}. \tag{2.26}$$

where $\dot{m}$ is the mass flow rate, T_0 is the total temperature, and p_0 is the total pressure. This formulation arises from the theory of choked (sonic) flow, in which $\dot{m}\sqrt{T_0}/(Ap_0)$ becomes nearly invariant at the throat. Provided that the gas properties are known, the normalized flow capacity serves as a direct measure of the turbine's swallowing capability, independent of detailed throat area measurement.

From a theoretical perspective, the definition and application of these parameters are essential for subsequent aerodynamic losses analysis, and guiding the design of turbine stages.

2.2 Preliminary Turbine Design

The objective of preliminary turbine design is to establish a rational foundation for the detailed design phase by estimating the appropriate type and number of stages, and by providing initial geometric definitions for each blade row. This process encompasses the determination of key dimensions, including hub, mean, and tip radii, as well as leading and trailing edge blade angles, blade count, and chord length.

Although these parameters are preliminary and subject to refinement, they must be sufficiently close to their optimal values to enable efficient progression into detailed design. Preliminary design does not resolve detailed blade profiling or incorporate full three-dimensional effects, but rather uses a combination of one-dimensional mean-line analysis and classical design relations to construct the general layout of the turbine flowpath [72].

2.2.1 1D mean-Line analysis

The mean-line method represents the fundamental starting point for turbine design, which allows rapid estimation of stage geometry and performance before more detailed analyses. This approach is predicated on the assumption that the flow properties at the mean radius are representative of the entire annulus, thereby enabling a one-dimensional treatment that neglects circumferential and radial gradients. This approximation is particularly valid when the tip-to-hub radius ratio is not excessively large, and provides reliable first-order estimates for the main design variables.

The primary objectives of 1D mean-line design and analysis are as follows:

- Decide key non-dimensional parameters, such as stage loading (ψ), flow coefficient (ϕ), and degree of reaction (Λ), which collectively govern stage work and flow turning;
- Acquire preliminary velocity triangles at the mean radius, which relate absolute, relative, and tangential velocity components throughout the stage;
- Generate initial meridional dimensions to be used in subsequent iterative design and optimization cycles.

The foundational input data for mean-line analysis typically include: prescribed mass flow rate ($\dot{m}$), inlet total pressure and temperature (p_0, T_0), stage pressure ratio, power output (P) or enthalpy drop (Δh_0), rotational speed (N), and target efficiency (η). Other geometric quantities, such as hub/tip radii, axial chord, pitch, and blade number, are estimated as part of the design process and subsequently refined.

The 1D design and analysis is an iterative process comprising several key steps, briefly described below. At the heart of mean-line calculations lies the velocity triangle, which defines the relationships between blade and flow velocities. The calculation workflow for 1D design includes the following steps:

Loading and flow coefficient selection The first step in mean-line analysis is to select an appropriate ψ and ϕ. ψ is typically selected using the Smith chart or similar empirical tools. The process begins by calculating N_s based on the target total enthalpy drop, rotational speed, and mass flow rate. Using this value, a suitable ψ range is identified near the efficiency peak on the Smith chart. To reduce the number of stages and simplify the system, a higher ψ is often chosen, for example, 0.7–0.9 for high-pressure (HP) stages in gas turbines. In contrast, to maximize the efficiency of individual stages, a lower ψ is preferred, typically 0.3 to 0.6 for low-pressure gas turbine (LP) stages. In steam turbines, HP stages, characterized by high steam density and short blade height, usually operate at a moderately low ψ (0.5–0.7). LP stages, which handle larger flow rates and involve more stages, tend to adopt even lower values (0.3–0.5).

Selection of reaction degree The degree of reaction has a major impact on blade geometry, stage performance, and thermal loading. As discussed earlier, careful selection of Λ can balance efficiency while minimizing thermal stress and aerodynamic losses.

Determination of number of stages The required number of stages (N) can be estimated from the available total enthalpy difference as:

$$N \geq \frac{\Delta h_0}{\psi \Sigma U^2}. \tag{2.27}$$

Higher ψ and U reduce the required number of stages but increase mechanical stresses and potential vibration issues. Multi-stage design therefore

requires careful trade-offs among these parameters, constrained by material properties, manufacturability, and performance limits. As mentioned earlier, the range of possible stage loadings is selected from the empirical Smith chart or Balje diagram corresponding to the specific speed [62].

Loss modeling and efficiency estimation Total-to-static isentropic efficiency (η_{ts}) can be analytically related to loss coefficients and stage kinematics [71]. For a single stage, η_{ts} can be written as:

$$\eta_{ts} = \frac{h_{01} - h_{03}}{h_{01} - h_{3ss}}. \tag{2.28}$$

Rearrangement yields:

$$\eta_{ts}^{-1} = 1 + \frac{1/2C_3^2 + (h_3 - h_{3s}) + (h_{3s} - h_{3ss})}{h_{01} - h_{03}}. \tag{2.29}$$

The stator and rotor losses can be separated and expressed via their respective loss coefficients, ζ_N and ζ_R, as

$$h_2 - h_{2s} = \frac{1}{2} C_2^2 \zeta_N, \tag{2.30}$$

$$h_3 - h_{3s} = \frac{1}{2} W_3^2 \zeta_R. \tag{2.31}$$

leading to:

$$\eta_{ts}^{-1} = 1 + \frac{\left(\frac{T_3}{T_2}\right) c_2^2 \zeta_N + W_3^2 \zeta_R + c_3^2}{2(h_{01} - h_{03})}. \tag{2.32}$$

This formalism enables the estimation of efficiency and supports the rapid assessment of design choices against loss mechanisms identified in empirical correlations and validated models.

Estimation of geometrical dimensions The specific speed definitions using the actual specific work output for compressible flow can be obtained as below:

$$N_s = \frac{\omega\sqrt{Q}}{(\Delta h_0)^{3/4}}. \tag{2.33}$$

Here, Δh_0 refers to the specific enthalpy drop per stage, evaluated at design conditions. Q denotes the volumetric flow rate. Next, consult the Cordier

chart [62] (or the empirical N_s–D_s relationship) to obtain the specific diameter D_s, and then back-calculate the mean diameter:

$$D = D_s \frac{\sqrt{Q}}{(\Delta h_0)^{1/4}}. \tag{2.34}$$

Choose a typical hub-to-tip ratio γ, obtain the tip radius $r_{\mathrm{t}} = D/2$ and hub radius $r_{\mathrm{h}} = \gamma\, r_{\mathrm{tip}}$, and compute the mean radius r_{mean} (e.g., as the geometric mean):

$$r_{\mathrm{m}} = \frac{r_{\mathrm{h}} + r_{\mathrm{t}}}{2}. \tag{2.35}$$

Mass conservation in a turbine annulus is given by:

$$\dot{m} = \rho A_x C_x. \tag{2.36}$$

where C_x is the axial component of the absolute velocity, and $A_x$is the cross-sectional flow area normal to that axis, which can be estimated as:

$$A_x \approx 2\pi r_m H. \tag{2.37}$$

with r_m. The blade height H is then given by:

$$H = \frac{\dot{m}}{\rho r_m C_x 2\pi}. \tag{2.38}$$

The aspect ratio (height to axial chord) is commonly used to guide blade and vane chord selection, given as:

$$\text{Aspect ratio} = \frac{H}{b}. \tag{2.39}$$

where b is the axial blade chord length. While primarily determined by mechanical and manufacturing constraints, aspect ratios for modern turbines are guided by empirical best practices and aerodynamic considerations.

Zweifel criterion and blade solidity To further optimize turbine performance characteristics, the Zweifel criterion (Zweifel coefficient, Z_w) [73] is widely used to establish the optimal pitch-to-chord ratio (s/b) and corresponding blade solidity ($\sigma = b/s$):

$$Z_w = 2\frac{s}{b}\cos^2 a_2(\tan a_1 + \tan a_2). \tag{2.40}$$

where s is the blade pitch (spacing), a_1 and a_2 are the inlet and outlet flow angles.

The Zweifel criterion identifies the point of minimum aerodynamic loss by balancing the trade-off between close blade spacing (which increases frictional losses) and wide spacing (which promotes flow separation on the suction side). To ensure efficient flow control and avoid excessive aerodynamic loading, it is industry best practice to check that the initial solidity satisfies the Zweifel factor levels of approximately 1.05 at the hub and 0.8 at the tip. Furthermore, the Zweifel factor should generally be maintained below 1.2 throughout the span to prevent aero overloading, which could otherwise lead to increased losses and reduced stage efficiency. Once the solidity $\sigma = b/s$ is chosen, the pitch s is determined accordingly, and the number of blades is then calculated as:

$$Z = \frac{2\pi r_m}{s}. \tag{2.41}$$

The number of blades and the degree of reaction are inherently interrelated in their influence on loss mechanisms and flow control. Increasing the blade count generally reduces the aerodynamic loading on each blade, improves flow turning, and helps suppress secondary flow losses. However, a higher blade number also increases the wetted surface area, leading to greater skin-friction losses, as well as higher mechanical mass and centrifugal stresses. An excessive number of blades may introduce structural complications and increase the risk of vibration, whereas too few blades result in higher blade loading and greater endwall and secondary flow losses.

Reaction optimization Reducing reaction at constant blade number lowers rotor blade temperature, advantageous for high-temperature operation, while reducing blade number at fixed reaction increases blade loading and stagger, complicating platform integration and potentially raising endwall loss. The design process must therefore utilize iterative mean-line studies and graphical optimization techniques (such as constant reaction and Zweifel criterion curves) to identify the most advantageous trade-off among aerodynamic efficiency [71].

2.2.2 Loss model

Preliminary loss models play a crucial role in axial turbine design by linking thermodynamic performance objectives to geometric and aerodynamic parameters [74]. While detailed three-dimensional simulations may be unavailable during early mean-line or through-flow analyses, accurate loss

estimates are essential for predicting stage efficiency, work output, and for guiding initial sizing decisions.

1. Sources of aerodynamic loss A loss modeling approach begins by identifying the principal loss-generating mechanisms in the turbine flowpath. Advanced software tools classify losses into physically and empirically distinct categories that enable modular analysis, empirical calibration, and targeted design improvement. Although all aerodynamic losses are interconnected through viscous and turbulent interactions, they are commonly classified into several categories for engineering analysis:

- **Profile Loss**: Originates from skin friction and boundary layer development along the blade surfaces, and is sensitive to Reynolds number, surface roughness, and Mach number. It is typically dominant at mid-span and is directly influenced by blade shape, camber, and surface quality [70, 75].
- **Trailing Edge Loss**: Results from the wake and flow separation behind the blade trailing edge, encompassing both mixing and sudden expansion losses as the wake merges with the mainstream flow [76].
- **Secondary Flow Loss**: Driven by cross-passage pressure gradients, especially near endwalls, leading to the passage vortices. These losses are particularly significant in low aspect-ratio blades, where endwall boundary layers and pressure-driven vortices occupy a larger fraction of the flow passage. Low aspect-ratio means the blade height is small, so the flow near the endwalls occupies a larger proportion of the passage. The pressure gradients across the passage cause fluid to move from high-pressure to low-pressure regions near the endwalls, forming strong secondary vortices, which increase mixing of high-energy core flow with low-energy boundary layer flow near the walls, increasing turbulence and viscous dissipation, which causes energy loss [70, 74].
- **Endwall (Annulus) Loss**: Generated by viscous effects and boundary layer growth on the endwalls, often overlapping with secondary losses and sensitive to tip clearance and spanwise pressure gradients [77].
- **Tip Clearance Loss**: Caused by leakage flows between the blade tip and casing, forming strong vortical structures and additional mixing

losses. Tip leakage is especially problematic in unshrouded rotors and for high-reaction stages [78].

- **Incidence Loss and Deviation Loss**: Incidence loss reflects a mismatch between the inflow angle and the blade leading edge metal angle, with strong asymmetry between positive and negative incidence due to suction/pressure side separation characteristics. The curve of incidence loss as a function of angle is shown schematically in Figure 2.5. Incidence loss increases faster for positive angles due to rapid thickening of the suction surface boundary layer at positive stalling. Turbine blades generally tolerate negative incidence better until flow separation occurs on the pressure side. Deviation loss is the difference between geometric and flow exit angles, influenced by profile shape, loading, and flow conditions. Both are addressed in modern correlations and off-design corrections [69].
- **Shock and Transonic Loss**: In high-speed turbines, additional losses arise from shock formation, supersonic expansion, and non-ideal mixing. These are addressed via specialized transonic/supersonic loss models [79].
- **Other Specialized Losses**: Partial admission (e.g., Traupel, Frolov, Sheglyaev), wetness effects (for steam turbines), cooled flow mixing, and disk friction are treated as additional terms or integrated models, especially in comprehensive industry-standard codes [80].
- **Empirical Whole-Blade Loss Estimates**: For rapid preliminary assessment where detailed decomposition is impractical, overall loss correlations such as Soderberg, Smith or Latimer can be used. These "black-box" models provide a single-value loss estimate but lack component-level insight [81].

2. Loss model implementation in 1D Mean-Line design The loss model integrates four complementary correlations to capture all major loss mechanisms in axial turbine stages: AMDC (Ainley–Mathieson with Dunham–Came corrections) [82] for profile and trailing-edge losses; KO (Kacker–Okapuu) [83] for secondary-flow and endwall effects; MK (Moustapha–Kacker) [84] for tip-clearance losses; and BSM (Boundary-Separation Model) [85] for separation losses under off-design conditions. Together, they account for Mach and Reynolds number effects, blade loading, tip clearance, three-dimensional flow, incidence, shocks, choking, wetness, cooling, disk friction, and partial admission.

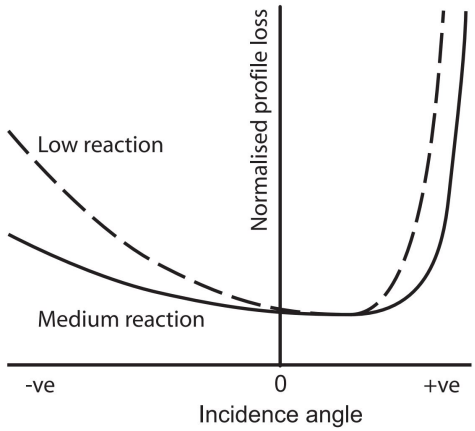

Figure 2.5: Rotor incidence loss characteristics for stages with different reaction levels. The curves show normalized profile loss as a function of incidence angle for low-reaction (dashed line) and medium-reaction (solid line) stages.

Implemented on a modular blade-row basis, the model allows stage-specific and spanwise variation of parameters, and is validated against CFD, experimental data, and industry benchmarks [86–88]. The selection and integration of these correlations, in combination with ϕ, ψ, and reaction, determine the predictive accuracy of mean-line analysis and the attainable efficiency and robustness of the turbine.

2.2.3 Through-flow analysis

The preliminary design of axial turbines begins with a mean-line analysis, which provides initial estimates of blade loading, flow angles, and velocity triangles at the mean radius. However, this one-dimensional approach is inherently limited: it cannot account for radial gradients in velocity, pressure, and blade speed that fundamentally affect real turbine operation. To overcome these limitations and achieve reliable, manufacturable blade designs, two-dimensional through-flow analysis in the meridional plane is employed.

Theory and methodology Through-flow analysis [89] addresses the coupled variation of flow properties along the span, reflecting the effects of centrifugal force, radial pressure gradients, and blade curvature. Several approaches exist: The first is Multi-streamline mean-line analysis: Repeats 1D mean-line calculation at multiple spanwise stations (hub, mid,

tip), applying empirical corrections for secondary flows and tip leakage. While simple, this approach relies heavily on correction factors and cannot resolve true spanwise flow structures. Next is the Streamline curvature method: The industry-standard for preliminary through-flow design. The inviscid, axisymmetric Euler equations are solved in the meridional plane along quasi-orthogonal streamlines, with blockage factors and empirical loss/deviation correlations included to approximate viscous effects. This method offers an effective compromise between fidelity and computational speed, guiding initial blade profile shaping from hub to tip. Last is the Full Euler/Navier-Stokes methods: High-fidelity CFD, directly solving for 2D or 3D flow fields. These approaches capture detailed loss mechanisms and secondary flows but require detailed geometry and significant computational resources, making them impractical for early-stage design.

In axial turbine stages, the radial velocity component C_r is usually much smaller than the other velocity components. Under steady, adiabatic conditions with no radial temperature gradients and no body-force terms, and if the total enthalpy h_0 and entropy s are assumed constant with radius, the radial equilibrium equation reduces to:

$$C_\theta \frac{\partial C_\theta}{\partial r} + \frac{C_\theta^2}{r} + C_x \frac{\partial C_x}{\partial r} = 0. \tag{2.42}$$

This equation reflects the balance of centrifugal and radial pressure forces in swirling flows, and is foundational for the prediction of spanwise variations in loading, reaction, and swirl angle distributions.

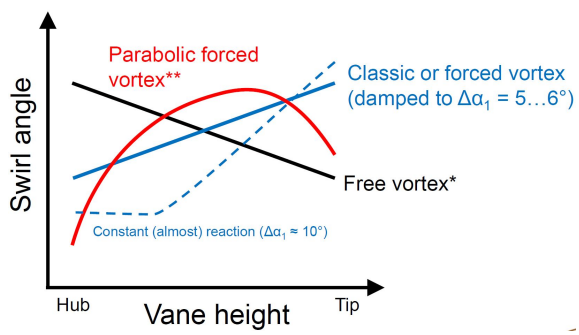

Figure 2.6: Schematic of different swirl distribution philosophies in axial turbine design. Swirl angle variation with vane height is shown for: free vortex (black solid line), classic or forced vortex with damping $\Delta\alpha_1 \approx 5$–6° (blue solid line), constant (almost) reaction with $\Delta\alpha_1 \approx 10^\circ$ (blue dashed line), and parabolic forced vortex (red curve).

Vortex philosophy and swirl angle distribution Turbine designs have the free vortex law, in which $C_\theta r = const$, producing a monotonic decrease in swirl angle from hub to tip. However, this results in excessive hub loading and tip unloading, amplifying secondary flow losses and undermining efficiency. More advanced design philosophies employ forced vortex or parabolic forced vortex distributions. The former tailors the spanwise swirl angle to achieve nearly constant or optimized work extraction across the blade height (see Figure 2.6). The parabolic forced vortex, in particular, concentrates loading around mid-span, reducing endwall and tip losses while supporting structural robustness. Damped forced vortex designs introduce controlled gradients in swirl, limiting spanwise incidence and maintaining manageable reaction variations.

Theoretical and practical implications Modern through-flow analysis thus serves as a bridge from 1D mean-line theory to high-performance 3D blade geometry. It quantifies the interplay between aerodynamic loading, work extraction, and secondary losses along the span of reaction and loading. Integration of empirically validated vortex and loading distributions, as practiced in advanced software and as demonstrated in this study, ensures the resulting turbine designs are efficient under real-world conditions [62, 84].

Chapter 3

Airfoil design and optimization

This chapter presents the design and optimization of airfoil sections, the three-dimensional stacking procedure used to construct the blade from these sections, and the 2D and 3D flow-field analysis methods employed to evaluate both individual-section and overall aerodynamic performance.

3.1 Design objectives

3.1.1 Introduction

The design of turbine blades focuses on directing the working fluid efficiently through the passages, thereby achieving effective energy transformation while minimizing aerodynamic losses. The fundamental aerodynamic objectives are as follows: (1) the blade inlet and exit angles must be precisely matched to the flow angles defined by the velocity triangles, thereby minimizing incidence and deviation losses; (2) the throat area must be accurately controlled, particularly under choked flow conditions, to regulate mass flow and ensure stability; (3) the blade passages should incorporate a smooth and gradual contraction of cross-sectional area to accelerate the flow while avoiding separation; (4) the blade surface curvature, along with its rate of change, should be maintained within specified limits to prevent adverse pressure gradients and boundary-layer separation; and (5) the static-pressure distribution along the blade surfaces should be optimized to

maximize work extraction while maintaining continuous flow attachment.

These interrelated objectives form the aerodynamic foundation for detailed profile development, optimization, and subsequent structural assessment.

3.1.2 Airfoil loading and diffusion factors

Blade loading, defined as the static pressure distribution along the blade surfaces, is a key aerodynamic parameter governing the tangential force F_t generated by turbine blades [65]. For a complete three-dimensional blade, F_t is obtained by integrating the local pressure difference between the pressure and suction surfaces over the blade surface projected in the tangential direction, which accounts for the radial variation of aerodynamic loading:

$$F_t = -\int_{\text{Area}} (p_{\text{PS}} - p_{\text{SS}})\, dA, \tag{3.1}$$

where p_{PS} and p_{SS} are the static pressures on the pressure and suction surfaces, respectively, and the integration is performed over the projected area in the tangential direction.

In practical blade design and analysis, the full 3D formulation is often replaced by a sectional approach for individual two-dimensional blade profiles. A common method is to use a blade loading diagram, which plots the static pressure difference between the pressure and suction sides as a function of surface distance along the profile, or equivalently in terms of a surface static pressure coefficient:

$$c_p = \frac{p - p_2}{p_{02} - p_2} \quad \text{or} \quad c_p = \frac{p_1 - p}{p_{01} - p_1}. \tag{3.2}$$

where p_2 and p_{02} are the exit static and total pressures, and p_1 and p_{01} are the inlet static and total pressures. Such diagrams provide a clear visualization of aerodynamic loading distribution and are widely used in both preliminary and detailed design to assess performance trends and identify separation risks.

For compressible flows [90], the isentropic Mach number M_{is} is often used as an alternative representation of surface pressure distribution. It is defined under the assumption of an isentropic process between the local static pressure and the inlet total pressure:

$$M_{\text{is}} = \sqrt{\frac{2}{k-1}\left[\left(\frac{p_{01}}{p_s}\right)^{(k-1)/k} - 1\right]}, \tag{3.3}$$

where p_{01} is the inlet total pressure, p_s is the local static pressure, and k is the specific heat ratio.

Optimal blade loading accelerates the flow along the suction side, reducing static pressure relative to the pressure side and thereby generating aerodynamic work. Near the leading edge, favorable pressure gradients are produced, while toward the trailing edge the high-velocity flow must be gradually decelerated to prevent excessive boundary-layer growth and separation.

The extent of this deceleration is characterized by the diffusion factor (DF), which measures the velocity reduction along the suction surface and serves as an indicator of separation risk and overall aerodynamic performance [65]. For compressible flows, the DF can be expressed in terms of isentropic Mach numbers following Mamaev [91]:

$$DF = \frac{M_{\text{max}} - M_{\text{exit}}}{M_{\text{exit}}}, \tag{3.4}$$

where M_{max} is the peak isentropic Mach number on the suction surface and M_{exit} is that at the blade exit. Higher DF values correlate with increased separation risk and reduced efficiency.

In addition to limiting the maximum DF, it is essential to ensure that diffusion occurs over a sufficient portion of the suction surface to avoid localized rapid deceleration. This is quantified by the diffusion-rate parameter:

$$\text{Rate parameter} = \frac{\Delta l_{\text{diffusion}}}{l_{\text{SS}}}, \tag{3.5}$$

where l_{SS} is the suction-surface arc length and $\Delta l_{\text{diffusion}}$ is the length of the diffusion region. Empirical correlations suggest constraining this parameter to ≤ 0.6 for subsonic and transonic turbine blades to maintain gradual deceleration and prevent flow separation [91].

3.1.3 Front-loaded vs. aft-loaded

The spanwise and chordwise distribution of aerodynamic loading on turbine blades strongly influences boundary-layer development, aerodynamic losses, and thermal behavior. Figure 3.1 compares the characteristic features of front-loaded and aft-loaded blade designs, highlighting their implications for different Reynolds number regimes and associated flow physics [65].

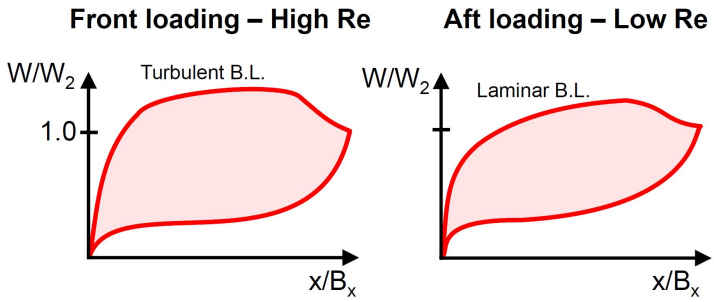

Figure 3.1: Comparison of front-loaded and aft-loaded blade designs. Velocity distributions along the suction surface are plotted as normalized velocity W/W_2 versus normalized axial chord x/B_x. (a) Front-loaded profile at high Reynolds number with predominantly turbulent boundary layer; (b) aft-loaded profile at low Reynolds number with predominantly laminar boundary layer [92].

Front-loaded blades concentrate aerodynamic loading near the leading edge, producing an early peak in the suction-side pressure distribution. This approach is advantageous at high Reynolds numbers, where rapid transition to a turbulent boundary layer enhances flow stability and resistance to separation [93, 94]. Early transition reduces the risk of laminar separation bubbles and supports robust operation under varying incidence conditions. However, a longer chordwise extent of turbulent flow increases skin-friction losses and elevates heat-transfer rates at the leading edge, intensifying cooling requirements and potentially amplifying thermal gradients and material stresses.

In contrast, **aft-loaded blades** shift the primary loading peak towards the trailing edge, extending the laminar-flow region along the suction surface. This configuration is well-suited to low Reynolds number regimes, such as those in rear stages or smaller turbines [92]. Benefits include reduced profile-friction losses, lower leading-edge heat-transfer coefficients, and the potential for reduced secondary-flow and passage-vortex losses. However, aft-loaded designs are more susceptible to flow separation and stall due to a higher diffusion rate over a shorter chordwise distance.

In all studies presented in this work, aft-loading was adopted as the baseline strategy for the following reasons:

- Maximize the extent of laminar boundary layer to minimize profile-friction losses.
- Lower local heat-transfer coefficients at the leading edge, reducing cooling-system complexity and improving material life.

- Enhance overall aerodynamic efficiency by suppressing secondary losses and optimizing endwall flow behavior.

Although aft-loading offers substantial benefits in terms of loss reduction and thermal management, its success depends critically on careful control of pressure recovery and surface diffusion parameters, which can be readily quantified and optimized in modern blade-design workflows.

3.2 Design and optimization of airfoil sections

3.2.1 Design of airfoil sections

The design of airfoil sections begins with determining the required number of sections and their spanwise locations. A common approach is to define sections at the hub, mean (midspan), and tip, as illustrated in Figure 3.2. However, the combined effects of stress and temperature may cause the life-limiting section to occur at an intermediate spanwise position; in such cases, the local cross-sectional area must be adjusted to meet the blade life target. The axial spacing between successive blade rows is influenced by both aerodynamic and mechanical considerations and is usually minimized to meet blade life requirements, typically set to about 20%–35% of the axial chord length of the upstream blade [62].

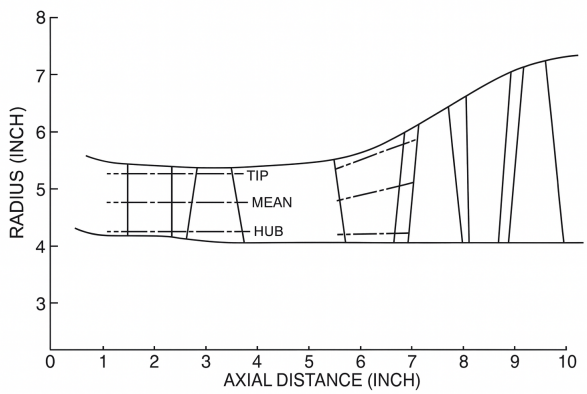

Figure 3.2: Meridional diagram showing blade section lines [62].

Several methods are available for constructing blade sections, including simple geometric constructions, camberline–thickness methods, and parametric descriptions. The Pritchard method satisfies most design requirements

by calculating the pressure and suction surfaces from specified parameters, combining third-order polynomials and circular-arc segments, and ensuring first-derivative continuity at all blend points to maintain smooth slope transitions. However, this and similar parameterizations do not guarantee second-derivative continuity, and surface curvature discontinuities may occur. Modern airfoil section generators often use Bézier curves to define the pressure and suction surfaces, providing greater geometric flexibility while maintaining a high degree of continuity in both the curves and their derivatives [65].

3.2.2 Optimization of airfoil sections

Curvature-controlled blade construction is a modern approach for generating smooth, aerodynamically optimized blade profiles by prescribing curvature distributions instead of directly defining surface coordinates. This methodology has been widely integrated into advanced turbomachinery design software such as AxCent, enabling robust aerodynamic shaping and efficient numerical optimization [95, 96].

A. Aerodynamic and practical advantages

The curvature-controlled method produces blade profiles with continuous curvature and favorable pressure gradients, enhancing boundary-layer stability, reducing separation risk, and providing precise control over leading- and trailing-edge features, wedge angles, and throat width [97]. The approach is robust in automated optimization and inherently avoids undesirable inflection points or abrupt curvature variations common in traditional Bézier- or spline-based parameterizations. It supports shaping of both suction and pressure sides, and can naturally accommodate special cases such as straight-line transitions or extended regions of zero curvature.

B. Optimization strategies for target Mach distribution

Effective application of curvature-controlled methods requires careful tuning of curvature in distinct chordwise regions to achieve a target Mach number distribution. Near the leading edge, curvature should be modest and smoothly varying to promote gradual acceleration, while excessive positive curvature can induce premature acceleration or local shock formation. In the mid-chord region, maintaining relatively uniform negative curvature supports a stable pressure gradient, minimizing sharp Mach peaks or flow instabilities. Toward the trailing edge, curvature should smoothly approach

zero to form a controlled deceleration zone; abrupt changes here may provoke adverse pressure gradients and separation [98].

Excessive deceleration on the suction surface can lead to local shock formation, causing strong pressure jumps and flow separation, which significantly increase aerodynamic losses. Maintaining smooth curvature transitions controls the pressure gradient and helps avoid shock-induced performance degradation. Parameterized curvature functions (splines or Bezier) are iteratively adjusted to satisfy aerodynamic constraints while preventing deleterious shock effects, enabling robust optimization of turbine blade profiles.

3.2.3 Aerodynamic optimization of blade profiles

Blade aerodynamic performance is fundamentally governed by the interplay between surface pressure gradients, boundary-layer evolution, and profile-induced flow deviation. Three classical performance parameters are widely used as quantitative guidelines for the aerodynamic design and multi-objective optimization of turbine blades: suction-surface diffusion, profile loss (characterized by the diffusion-rate parameter), and uncovered turning.

Suction-surface diffusion is a critical parameter for controlling boundary-layer separation and minimizing overall loss. As established by Mamaev [91] and adopted in both academic and industrial practice, the optimal suction-side diffusion factor D_{SS}^{Opt} decreases monotonically with increasing exit Mach number M_{exit}, due to the need to limit adverse pressure gradients and maintain attached flow. This relationship, given in Equation 3.4 and shown in Figure 3.3, serves as a rapid screening tool in early-stage design for keeping flow deceleration within empirically validated limits.

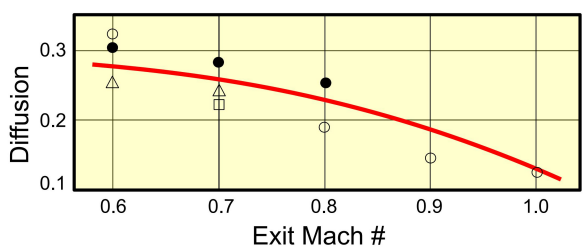

Figure 3.3: Empirical Correlation of Optimal Suction-Surface Diffusion Coefficient with Exit Mach Number, adapted from Mamaev [91].

Diffusion rate parameter is based on the diffusion concept of the suction surface by incorporating not only the magnitude but also the spatial extent of the adverse pressure gradients. As shown in Equation 3.5, the higher diffusion rate parameters are strongly correlated with an increase in the profile loss coefficient Y_p (Figure 3.4), with losses rising dramatically when the parameter exceeds 0.5–0.6 [99]. Modern design therefore aims to maintain this parameter below the threshold to minimize energy losses and reduce the risk of separation. Compared with suction surface diffusion, which mainly reflects the allowable peak adverse pressure gradient, the diffusion rate parameter provides a more comprehensive measure by also accounting for the spatial extent of the gradient along the suction surface.

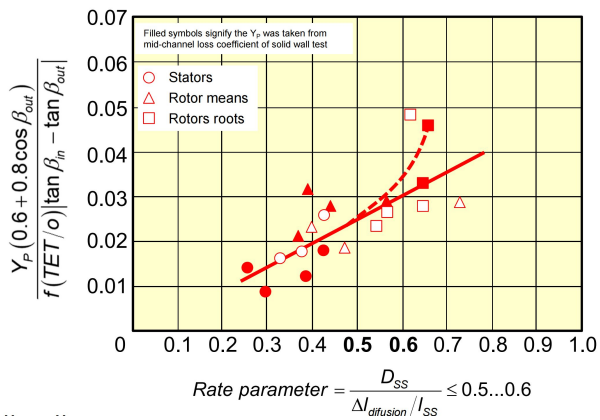

Figure 3.4: Profile loss coefficient as a function of the diffusion-rate parameter [91]. Filled symbols indicate loss coefficient values obtained from mid-channel solid-wall tests. The red line represents the fitted trend.

Uncovered turning refers to the portion of flow turning that occurs upstream of the blade leading edge on the suction-surface side, without direct guidance from the blade profile. Excessive uncovered turning imposes a strong local curvature on the incoming streamlines, leading to rapid acceleration along the suction surface. At high M_{exit}, this can drive the local Mach number at the throat to unity, causing shock formation and subsequent boundary-layer separation, both of which contribute to increased aerodynamic loss. Based on experimental correlations, Mamaev [91] proposed design limits for allowable uncovered turning as a function of M_{exit} and the blade exit metal angle β, with recommended values ranging from approximately 7° at high-speed conditions to 18° at low-speed operation (Figure 3.5).

In this study, these aerodynamic constraints were explicitly incorporated

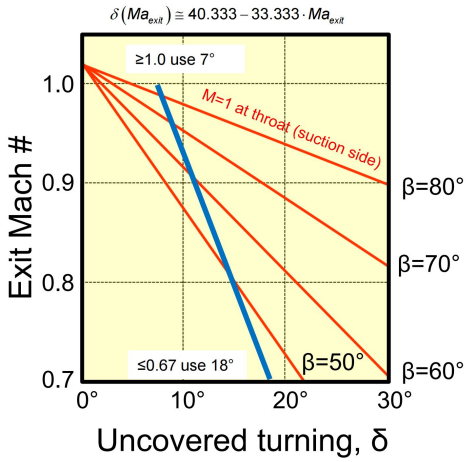

Figure 3.5: Recommended limits of uncovered turning δ as a function of exit Mach number M_{exit} and blade exit metal angle β, adapted from Mamaev [91]. The blue line indicates the empirical limit $\delta(M_{\text{exit}}) \approx 40.333 - 33.333 \cdot M_{\text{exit}}$, while the red lines mark the onset of $M = 1$ at the suction-surface throat for different β values.

into the blade optimization process. The target isentropic Mach number distribution (Figure 3.6) was defined to simultaneously satisfy diffusion limits, maintain favorable pressure gradients, and restrict uncovered turning, thereby ensuring a balance between aerodynamic efficiency and operational robustness.

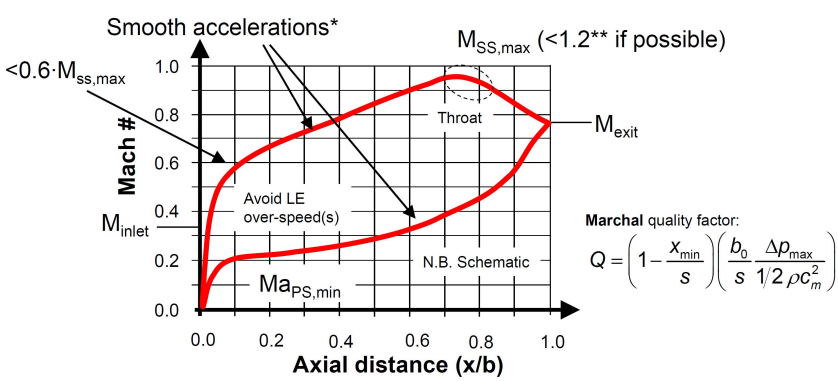

Figure 3.6: Target isentropic Mach number distribution for an aft-loaded turbine blade, showing the characteristic delayed suction-side peak and the design limits on peak Mach number, diffusion factor applied during optimization [91].

The primary optimization goals are summarized as follows:

- **Minimize total pressure loss:** Reduce aerodynamic losses across

the blade passage by controlling diffusion rates and avoiding shock formation on the suction surface.

- **Maintain boundary-layer stability:** Ensure continuous and smooth acceleration along the suction surface to minimize adverse pressure gradients and prevent boundary-layer separation. Shape the Mach number distribution to avoid leading-edge overspeeds and abrupt deceleration near the trailing edge.
- **Control maximum surface Mach number:** Based on aft-loading principles (Figure 3.6), maintain the maximum suction-surface Mach number ($M_{SS,\max}$) below 1.2 wherever possible to prevent local supersonic regions and associated shock-induced losses.
- **Manage diffusion factors:** Maintain D_{SS} within 0.20–0.25 and D_{PS} below 0.45 to limit boundary-layer thickening and separation. Constrain the diffusion rate parameter to ≤ 0.6 to ensure gradual and stable deceleration.
- **Optimize exit flow conditions:** As shown in Figure 3.7, the total entropy generation exhibits a minimum near the optimal exit Mach number $M_{\text{exit,opt}}$, where the balance between viscous and shock-related losses is most favorable. Maintaining the normalized exit Mach number $M_{\text{exit}}/M_{\text{exit,opt}}$ within the range of 0.9–1.0 minimizes entropy production and maximizes stage efficiency. Values significantly below this range increase viscous dissipation due to underloading, while excessive M_{exit} promotes local supersonic flow and shock formation on the suction surface, leading to a rapid rise in irreversibility.
- **Minimize entropy generation:** Steer designs toward operating conditions with lower $\Delta\zeta(M_{\text{exit}})/\zeta_{\text{opt}}$, directly reducing irreversible losses.
- **Ensure robustness across operating range:** Validate designs under both design and off-design conditions to ensure that performance deterioration under part-load or transient operation remains within acceptable limits.

Throughout the optimization process, all targets and constraints were continuously monitored and enforced via automated routines. This ensured consistent adherence to design objectives across the entire blade family, achieving a robust balance between aerodynamic efficiency, loss minimization, and operational flexibility.

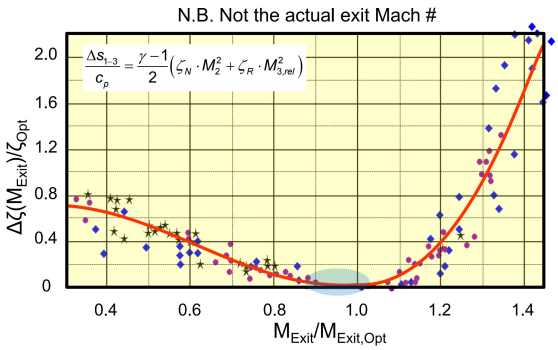

Figure 3.7: Correlation between normalized exit Mach number ($M_{\text{exit}}/M_{\text{exit,opt}}$) and entropy generation loss, showing the minimum-loss region near $M_{\text{exit}}/M_{\text{exit,opt}} \approx 1.0$.

3.3 Three-Dimensional design and analysis

3.3.1 Blade stacking and radial distribution

Blade stacking arranges two-dimensional blade sections along the span to form the three-dimensional geometry, with the stacking law strongly influencing aerodynamic efficiency, secondary-flow control, structural robustness, and manufacturability [100]. Several methods are commonly used and may be combined to balance performance and flow control (Figure 3.8).

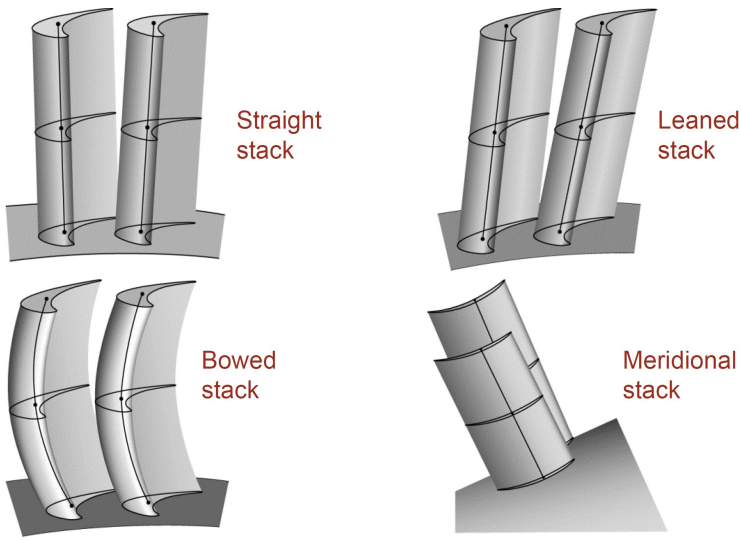

Figure 3.8: Common turbine blade stacking methods: straight, leaned, compound-lean, bowed, and meridional, each affecting spanwise load distribution and secondary-flow behavior differently [65].

Straight stacking aligns sections vertically, simplifying manufacture but often producing high hub-region loading and secondary-flow losses. **Leaned stacking** shifts sections tangentially; forward lean reduces hub losses, backward lean reduces tip losses [101]. **Compound lean** varies lean angle along the span, enabling finer control of load distribution and secondary-flow suppression [101]. **Bowed stacking** introduces both tangential and axial displacement, with forward bowing mitigating hub losses and backward bowing alleviating tip loading, at the cost of greater geometric complexity [65]. **Meridional stacking** offsets sections radially and axially to follow the annulus contour and local streamlines, improving flow uniformity but requiring advanced tools and careful structural integration [102].

3.3.2 Three-Dimensional CFD analysis

1D and 2D analyses provide essential insights during preliminary blade design. However, their inherent limitations prevent the accurate capture of complex three-dimensional flow phenomena, such as spanwise pressure gradients, secondary flows, and tip-clearance vortices. To address these limitations, high-fidelity 3D CFD simulations are employed as a core component of advanced blade development and validation.

In a 3D CFD framework, the complete blade geometry is discretized within a full-annulus or sectoral annular domain. The governing Navier–Stokes equations, typically solved using Reynolds-averaged Navier–Stokes (RANS) turbulence models, enable detailed prediction of boundary-layer development, separation, shock–boundary layer interactions, and secondary-flow structures that cannot be resolved by 1D or 2D methods. However, reliance solely on 2D optimization can lead to overprediction of aerodynamic performance and underestimation of losses, particularly in endwall regions. The primary advantage of 3D CFD lies in its ability to resolve realistic performance metrics, identify local loss mechanisms, and quantify flow nonuniformity across the span.

In this thesis, 3D CFD was used to validate and refine the blade designs generated from 1D and 2D methodologies. The results directly informed final geometry adjustments based on spanwise distributions of Mach number, pressure coefficient, and entropy generation. This multi-fidelity design approach ensured that the finalized blade geometry achieved both high aerodynamic efficiency and robust performance under realistic engine operating conditions.

Chapter 4

Methodology

This chapter describes the complete methodology adopted in this thesis, covering both the software-driven design workflow and the computational strategies for simulating internal flows in axial steam and gas turbines. It first outlines the overall design process implemented in the selected software, then presents the governing equations and turbulence models, followed by the blade geometries considered. Finally, it details the discretization schemes, solver settings, mesh generation techniques, and boundary conditions used in the numerical simulations.

4.1 Computational workflow for axial turbines

Building on the theoretical foundations established in Chapters 2 and 3, the present methodology implements the axial turbine design process using dedicated commercial software. This ensures that the key non-dimensional parameters, aerodynamic principles, and blade design criteria described earlier are applied systematically in a reproducible workflow. The overall process is illustrated in Figure 4.1.

The workflow proceeds as follows:

1. **1D mean-line design in AXIAL, Concepts NREC LLC, USA)** – The Reynolds number, axial chord, number of stages, flow coefficient, stage loading coefficient, and special configurations such as partial admission or supersonic stages are optimized to select the best

candidate. Use redesign mode to generate multiple flowpath configurations under consistent design rules, and analysis mode to produce performance maps over the operating range.

2. **2D blade-section optimization and 3D blade generation in AxCent, Concepts NREC LLC, USA)** – Transfer the case via the Agile interface, importing from AXIAL. Apply parameterized stacking and shaping to create the 3D geometry, optimize blade profiles based on curvature-controlled methods and 2D analysis, and perform targeted manual optimization to improve blade loading distributions and aerodynamic performance.

3. **CFD performance evaluation** – Analyze the validated 3D geometry using three solvers: built-in pbCFD (Pushbutton CFD, PBPlus) [95], ANSYS Fluent 19.1, and ANSYS CFX, providing both rapid checks and high-fidelity performance assessments.

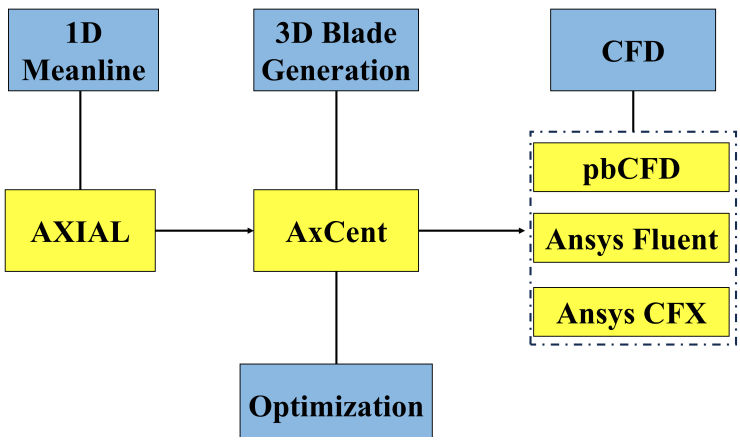

Figure 4.1: Schematic of the software-based axial turbine design workflow, showing sequential stages from 1D meanline design (selection of key non-dimensional parameters) to 2D blade-section optimization (curvature control and flow analysis), 3D geometry generation (stacking and shaping), and CFD performance evaluation.

Having described the practical implementation, the next section introduces the governing equations and numerical methods that underpin the simulations. This theoretical framework ensures that the computational predictions are physically consistent, accurate, and reliable.

4.2 Governing equations

The unsteady, compressible, and turbulent flows encountered in turbomachinery are governed by the Navier–Stokes equations, which encapsulate the conservation laws for mass, momentum, and energy [8]:

$$\frac{\partial \rho}{\partial t} + \frac{\partial (\rho u_i)}{\partial x_i} = 0, \tag{4.1}$$

$$\frac{\partial (\rho u_i)}{\partial t} + \frac{\partial (\rho u_i u_j)}{\partial x_j} = -\frac{\partial p}{\partial x_i} + \frac{\partial \tau_{ij}}{\partial x_j} + S_i, \tag{4.2}$$

$$\frac{\partial (\rho E)}{\partial t} + \frac{\partial (\rho u_i H)}{\partial x_i} = \frac{\partial (u_j \tau_{ij})}{\partial x_j} + \frac{\partial}{\partial x_i}\left(k \frac{\partial T}{\partial x_i}\right) + S. \tag{4.3}$$

where ρ is density, u_i velocity, p static pressure, τ_{ij} viscous stress tensor, E and H the total energy and enthalpy per unit mass, k thermal conductivity, T temperature, and S_i, S denote body force and heat source terms. The system is closed using the ideal-gas law,

$$p = \rho R T, \tag{4.4}$$

with R the specific gas constant [103]. Real-gas and steam effects are incorporated where necessary: in Paper I, with the working fluid modeled as steam under the ideal-gas assumption, while Papers II–IV utilize the ideal-gas assumption.

Turbulence is modeled via the Reynolds-Averaged Navier–Stokes (RANS) approach, in which the instantaneous velocity is decomposed as $u_i(t) = \bar{u}_i + u_i'(t)$. This introduces the Reynolds-stress tensor, modeled using the Boussinesq hypothesis [104]:

$$-\overline{u_i' u_j'} = \nu_t \left(\frac{\partial \bar{u}_i}{\partial x_j} + \frac{\partial \bar{u}_j}{\partial x_i}\right). \tag{4.5}$$

where ν_t is the eddy viscosity. Depending on case requirements, turbulence closure ranges from one- and two-equation models (e.g., k–ε, k–ω, SST) to advanced Reynolds Stress Models (RSM) [105].

RANS is selected for its proven accuracy and efficiency in predicting mean flowfields and performance in turbomachinery [106]. While higher-fidelity approaches such as LES and DNS can resolve a wider spectrum of turbulence scales, their prohibitive computational costs limit application to fundamental studies or single-passage investigations. For design and optimization cycles, RANS delivers the requisite balance of fidelity and computational traceability.

4.3 Geometry cases

4.3.1 2D blade profile cases

As part of the comprehensive computational framework established in this thesis, this section details the specific two-dimensional blade geometry configurations used for aerodynamic simulations and optimization studies. Four blade sections (Case 1 through Case 4) were constructed within the Concepts–AxCent environment, maintaining a constant chord length c while varying the inlet angle β_1 and outlet angle β_2. The specific geometric parameters for each case are summarized in Table 4.1, with corresponding blade profiles depicted in Figure 4.2. These geometry cases investigate the influence of inlet and outlet flow angles on curvature-controlled blade performance.

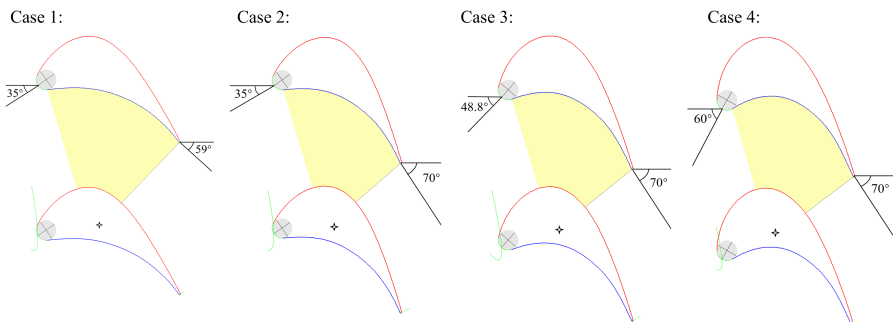

Figure 4.2: Schematic of blade sections for Case 1– Case 4. Inlet/outlet angles β_1, β_2 are indicated; 'yellow' region denotes the flow passage area between adjacent blades.

Table 4.1: Blade parameters for the four cases.

Parameters	Case1	Case2	Case3	Case4
$\beta_1(^\circ)$	35°	35°	48.8°	60°
$\beta_2(^\circ)$	59°	70°	70°	70°
Chord (m)	0.04187	0.04187	0.04187	0.04187
Stagger Angle(°)	–22.1	–31.8	–29.4	–27.9
Pitch/Chord	0.9574	0.9564	0.9569	0.9573
Gauge Angle(°)	56.8	66.7	66.7	66.7

It should be emphasized that these two-dimensional geometry configurations are the primary focus of the investigations in Papers II and III. Nevertheless, they also serve as the foundation for the blade aerodynamic optimization and flow analyses presented in Papers I and IV. These cases support the detailed parametric studies and CFD simulations carried out

in this thesis, offering valuable insights into the relationship between geometric parameters and aerodynamic performance.

4.3.2 Application cases in 3D axial steam and gas turbine geometry

While the 2D blade profiles described earlier are an essential element in the design process and serve as a key stage for optimizing aerodynamic performance, they do not capture radial flow variations, secondary flows, or endwall effects. To illustrate the application of the workflow to more realistic configurations, two representative 3D turbine geometries are presented here.

The first geometry, from Paper I, is a supersonic axial steam turbine designed using the established workflow. Its operating specifications are listed in Table 4.2, and the corresponding 3D configuration is shown in Figure 4.3.

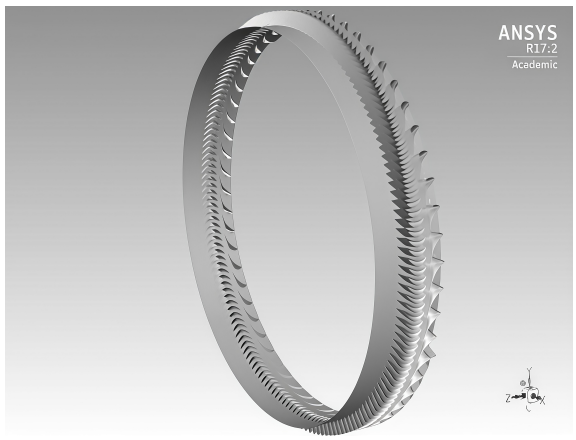

Figure 4.3: Schematic of axial steam turbine geometry from Paper I, generated using the integrated design workflow. The model shows the one-stage annulus blade row; see Table 4.2 for operating specifications.

Table 4.2: Specification for design of a supersonic steam turbine.

Parameter	Value	Description
Working media	H_2O	Steam
Power to grid	150 kW	Shaft Power 165–170 kW
Inlet temperature	173 °C	drop free
Inlet total pressure	850 kPa	
Outlet total pressure	140 kPa	
Mass Flow Rate	0.7–1 kg/s	
Shaft speed	18 000–36 000 rpm	

The second geometry, from Paper IV, is a 3D axial gas turbine generated during the design process. Due to confidentiality, only the geometric configuration is shown in Figure 4.4.

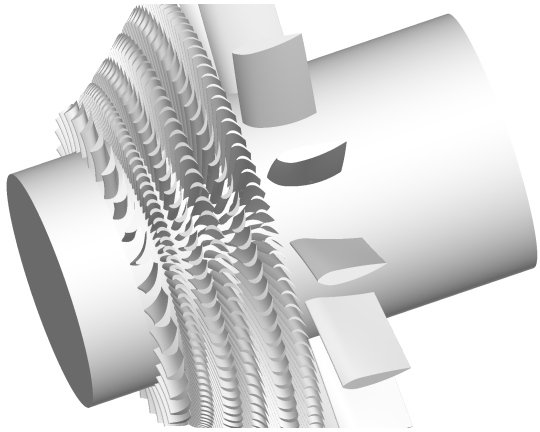

Figure 4.4: Schematic of 3D gas turbine geometry generated during the design process in paper IV.

4.4 Numerical methods

In the typical design process, pbCFD is employed for rapid validation of preliminary geometry and performance, providing quick feedback during the early design iterations. For refined analyses of critical sections, assessment of unsteady loading, and final verification, high-fidelity external solvers, ANSYS Fluent [107] and ANSYS CFX [108], are utilized.

4.4.1 Solver configuration

pbCFD is a multi-block Reynolds-Averaged Navier–Stokes (RANS) solver developed by Concepts NREC [95], offering three analysis levels for axial turbine flows: quasi-3D throughflow, B2B, and full 3D CFD. The quasi-3D method provides rapid prediction of radial flow distributions and stage matching, whereas the full 3D mode resolves secondary flows, tip leakage, and other complex three-dimensional phenomena. In this work, B2B analysis served as the primary tool for blade-shape optimization, striking a balance between computational cost and aerodynamic fidelity.

ANSYS CFX is a vertex-centered solver that solves the governing equations in a coupled manner at mesh nodes. Its streamline-based numerical meth-

ods generally achieve stable convergence in structured multistage turbomachinery simulations, particularly when used with high-quality meshes such as hexahedral or topologically similar grids. ANSYS Fluent, by contrast, is cell-centered and designed for greater flexibility in handling complex geometries and unstructured mesh topologies.

The CFX coupled solver is particularly efficient for steady multistage computations, while Fluent's versatility makes it well suited for problems involving shocks, multiphase flows, and irregular geometries. Solver selection in this thesis was based on physical modeling requirements:

- **Papers I–III:** ANSYS Fluent was chosen for its advanced shock-capturing and multiphase capabilities in the supersonic, partially admitted steam turbine (Paper I), and for efficient design iteration in two-dimensional cascades (Papers II and III).
- **Paper IV:** ANSYS CFX was adopted for accurate multistage, three-dimensional simulations using its fully coupled solver.

Across all cases, turbulence closure was provided by the SST k–ω model, selected for its demonstrated ability to predict boundary-layer separation and capture near-wall effects in turbomachinery flows. This model blends the k–ω formulation near walls with the k–ε approach in the free stream, offering both robustness and accuracy. Comparative assessments with the Realizable k–ε model in Paper II confirmed the SST model's superior performance in predicting boundary-layer development and separation.

Solver algorithms were tailored to the physical requirements of each case:

- **Paper I**: Transient PISO scheme in Fluent to resolve rotor–stator interaction effects.
- **Papers II–III**: Steady SIMPLE or coupled algorithms for efficient convergence in 2D optimization.
- **Paper IV**: Fully coupled steady-state solver in CFX for multistage 3D simulations.

Spatial discretization employed second-order central differencing for pressure and second-order upwind schemes for convection terms. For transient cases, second-order implicit backward-Euler integration was used to allow larger time steps without compromising accuracy.

4.4.2 Mesh generation and boundary conditions

High-quality structured meshes, combined with higher-order discretization schemes, improve both the convergence rate and the accuracy of CFD solutions. Mesh generation strategies were tailored to the specific requirements of each case study.

In **Paper I**, a high-resolution all-hexahedral mesh was generated, exceeding 200 million cells. O-, C-, and H-type block topologies were employed to ensure accurate resolution in critical flow regions, and mesh independence was confirmed through systematic sector-based studies.

In **Papers II and III**, structured quadrilateral meshes containing 110,000–120,000 cells were used for the 2D blade profiles. Near-wall refinement was applied to achieve $y^+ \approx 1$, ensuring accurate boundary layer resolution. An example of the meshes for these geometries is shown in Figure 4.5.

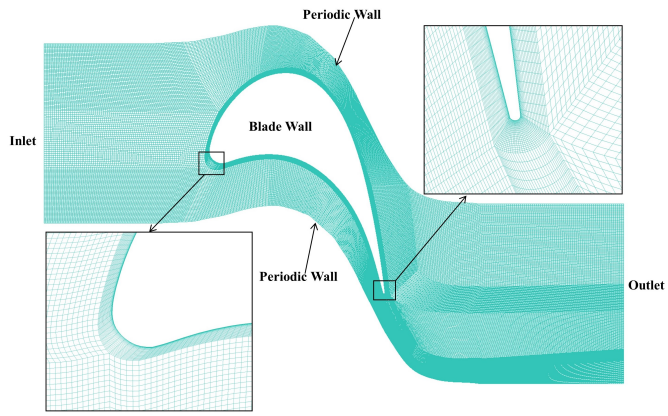

Figure 4.5: Structured mesh of the 2D turbine cascade computational domain, showing inlet, outlet, blade wall, and periodic boundaries. The two zoomed-in show near-wall mesh refinement around the blade surface and the smooth grid transition at the outlet.

In **Paper IV**, the mesh was initially generated in AxCent using O-, C-, and H-type block structures. Given the circumferential periodicity of each blade row in the full-annulus multi-stage axial turbine geometry, only a single channel sector as illustrated in Figure 4.6. The final computational grid comprised approximately 66.1 million nodes and 62.5 million elements in total.

Boundary conditions were assigned according to each case's design specifications:

Figure 4.6: Structured O, C, and H-type mesh topology for the computational domain of the multistage axial gas turbine in Paper IV, showing one channel passage; the final full-annual 3D mesh contained approximately 66.1 million nodes and 62.5 million elements.

- **Paper I**: Inlet total pressure and total temperature, outlet static pressure, adiabatic no-slip walls, and circumferential periodic interfaces to exploit geometric periodicity. Rotor–stator interaction was modeled using the frozen rotor approach to efficiently represent relative motion between blade rows.
- **Papers II and III**: Inlet total pressure and total temperature, outlet static pressure, and adiabatic no-slip walls applied to all blade and endwall surfaces. Circumferential periodic boundary conditions were imposed to represent the annulus sector.
- **Paper IV**: Inlet total pressure and total temperature, outlet static pressure, and adiabatic no-slip walls.

In summary, this chapter outlined the workflow from 1D mean-line design to 2D and 3D blade geometry generation and CFD analysis, establishing the methodological foundation for the results presented in Chapter 5.

Chapter 5

Results and discussion

In this chapter, the focus shifts to summarizing the most important results and discussions from the associated papers. The chapter is divided into two major sections: the first focuses on two-dimensional turbine blade investigations and aerodynamic performance optimization, while the second applies the turbine design framework to two applications (a shipboard steam turbine and a turbofan gas turbine), covering the entire process from preliminary design to in-depth three-dimensional flow characterization.

5.1 2D airfoil aerodynamic performance analysis and optimization

This section presents the results of evaluating various solvers and turbulence models for two-dimensional blade simulations. The discussion illustrates the selection of the most suitable model for simulating the effects of blade parameters and curvature distributions on aerodynamic performance, such as flow separation and shock losses.

5.1.1 Conclusions on solver–turbulence model combinations

In the 2D blade aerodynamic performance verification section of this study, a systematic comparison was conducted between different solvers (density-based and pressure-based) and turbulence models (Realizable k–ε and SST k–ω) to evaluate their differences in predictive performance at various Mach

numbers. This analysis not only validates the reliability of the numerical methods but also provides a modeling basis for the subsequent optimization and three-dimensional design.

The investigation concentrated on two representative operating conditions: a high-Mach case ($Ma = 1.10$) and a low-Mach case ($Ma = 0.76$), with corresponding Mach-number contours presented in Figure 5.1 and Figure 5.2. The accuracy of the numerical simulations was assessed through validation against the experimental measurements in Figure 5.3.

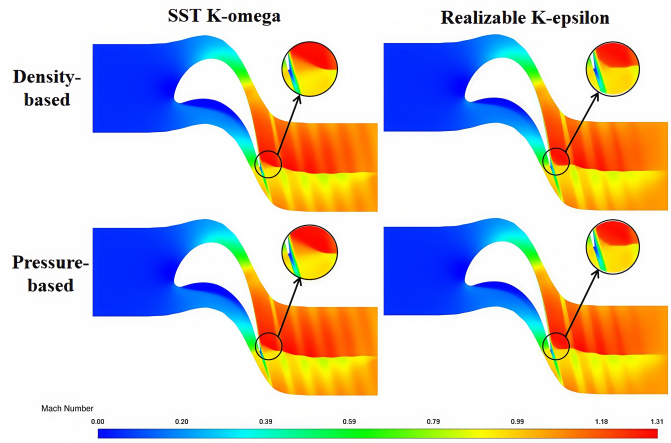

Figure 5.1: Mach number contours for four solver–turbulence model combinations (exit Mach number = 1.1). Top row: density-based solver; bottom row: pressure-based solver. Left column: SST k–ω model; right column: Realizable k–ε model. Zoom-in parts show the shock wave region.

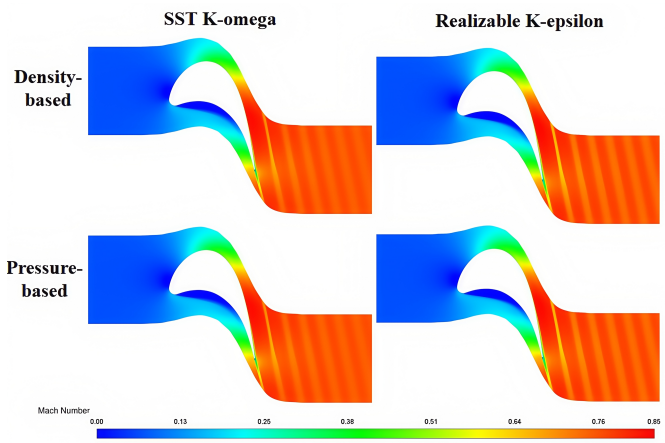

Figure 5.2: Mach number contours for four solver–turbulence model combinations (exit Mach number = 0.76). Top row: density-based solver; bottom row: pressure-based solver. Left column: SST k–ω model; right column: Realizable k–ε model. Zoom-in parts show the shock wave region.

When Ma is 1.10, as shown in Figure 5.1, both density-based and pressure-based Realizable k–ε models successfully captured the strong shock at the correct location, whereas the SST k–ω models demonstrate superior shock-capturing capability and more accurate prediction of near-wall shock interactions, making it the preferred choice for high-Mach cases. In contrast, when Ma is 0.76, as shown in Figure 5.2, all four solver–model combinations present similar Mach-number contours, with no significant differences in flow structure and no shock wave present, indicating that under such subsonic conditions the numerical results are largely insensitive to the choice of solver and turbulence model.

The validation results, shown in Figure 5.3, indicate that the numerical predictions are generally consistent with the experimental data, with differences remaining within a reasonable range. When the exit Mach number is below approximately 0.9, the total pressure loss remains low; beyond 0.9, the loss rises sharply due to the formation of shocks within the blade passage. The differences between the four turbulence-model–solver combinations are small: the density-based and pressure-based SST k–ω models yield similar results, as do the density-based and pressure-based Realizable k–ε models. When the Mach number exceeds about 1.05, the Realizable k–ε models show less variation than the SST k–ω models; however, in terms of growth trend, the SST k–ω models agree more closely with the experimental data.

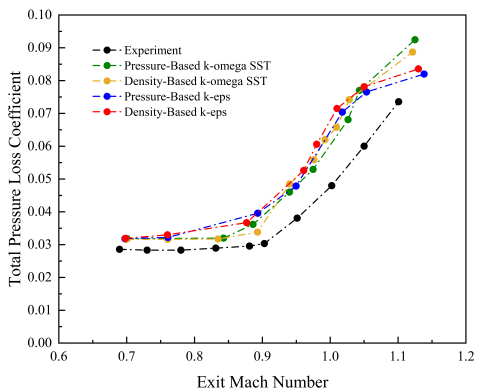

Figure 5.3: Variation of total pressure loss coefficient with exit Mach number for different CFD solver and turbulence model combinations, compared with experimental measurements. Black symbols: experiment; dashed/dotted lines: CFD predictions using pressure-based and density-based solvers with k–ω SST and k–ε turbulence model.

The discrepancies between the numerical and experimental results are mainly attributable to differences in shock-capturing capability and compressibility treatment, the inability of the present two-dimensional simu-

lations to resolve three-dimensional effects such as vortices and spanwise dissipation, the influence of the constant static-pressure outlet condition, differences in measurement methodology, and the inherent difficulty of accurately predicting transonic turbine flows (exit Mach 0.7–1.1) with RANS models.

5.1.2 Conclusions on surface curvature distribution and optimization on blade performance

With the numerical methodology validated in Section 5.1.1, this part of the study investigates the impact of blade surface curvature distributions on aerodynamic performance. A family of baseline blade profiles was generated under different inlet–outlet angle configurations, and each was subsequently optimized using a curvature-controlled Bezier-curve method.

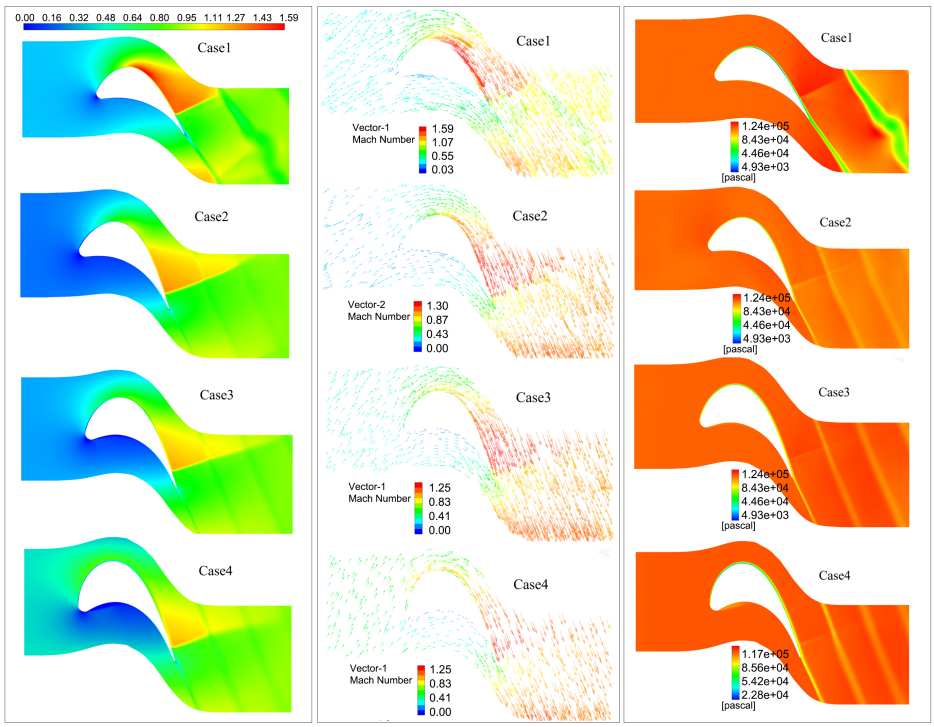

Figure 5.4: Comparison of flow fields for four design cases (Case 1–Case 4) when the Exit Mach Number is 0.94. (a) Relative Mach number contours; (b) Velocity vectors colored by relative Mach number; (c) Static pressure distribution (Pa).

As illustrated in Figures 5.4 and 5.5, the Mach number, velocity vectors,

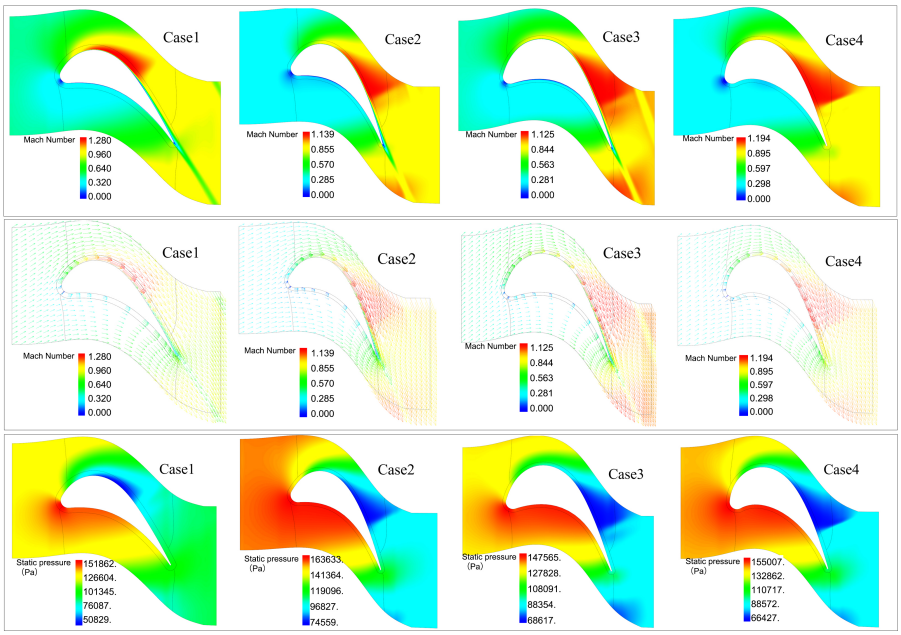

Figure 5.5: Contours for Four Optimized Cases (Case 1–Case 4) when the Exit Mach Number is 0.94. Top row: relative Mach number contours; middle row: velocity vectors colored by relative Mach number; bottom row: static pressure distribution (Pa).

and static pressure contours are compared before and after optimization for the family of blade profiles.The flow field contours for the original blade geometries in Figure 5.4 show that different blade profiles with different curvature distributions have a clear effect on the location and intensity of the shock waves, as well as on the structure of the wake. In particular, front-loaded designs produce higher peak Mach numbers in the mid-chord region, leading to stronger shocks and thicker wakes downstream. These features contribute to higher profile losses and reduced aerodynamic efficiency. After optimization, as shown in Figure 5.5, the loading distribution is shifted downstream. This reduces the peak Mach number, weakens shock intensity, and yields a more uniform static-pressure recovery. The wake region behind the trailing edge then becomes narrower and less pronounced, indicating reduced energy loss.

The curvature comparison in Figure 5.6 shows that optimization generally produces smoother curvature transitions on both suction and pressure surfaces. For the suction side, the curvature peaks are moderated and shifted slightly upstream, thereby alleviating adverse pressure gradients. On the pressure side, the curvature troughs are deepened and shifted toward the leading edge, promoting earlier flow acceleration. These changes collec-

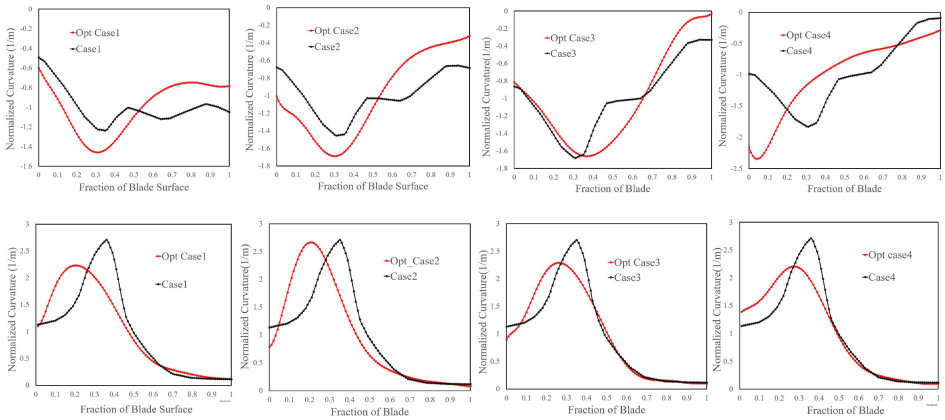

Figure 5.6: Comparison of normalized curvature distributions along the blade surfaces for original and optimized designs in four cases (Case 1–Case 4). Top row: suction-side surface curvature; bottom row: pressure-side surface curvature. Curvature is normalized by blade chord length, and the horizontal axis represents the fractional distance along each surface from the leading edge to the trailing edge.

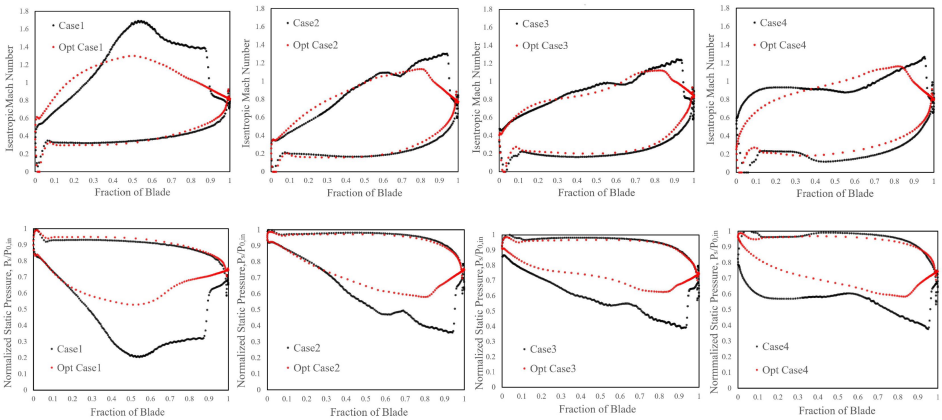

Figure 5.7: Comparison of blade surface aerodynamic distributions for original and optimized designs in four cases (Case 1–Case 4). Top row: isentropic Mach number along the blade surface; bottom row: normalized static pressure p/p_{in} along the blade surface. The horizontal axis represents the fractional distance from the leading edge to the trailing edge.

tively contribute to a more favorable aerodynamic loading pattern.

The corresponding loading distributions, as shown in Figure 5.7, confirm this trend. In the optimized profiles, the peak isentropic Mach number is reduced and often shifted downstream compared with the baseline, weakening shock intensity and reducing associated losses. Static-pressure recovery is also more uniform, with the steep drops and rebounds near the trailing edge in the baseline designs largely eliminated after optimization.

Across the tested outlet Mach-number range, the optimized blades consis-

tently achieved lower profile-loss coefficients and reduced diffusion factors. A lower diffusion factor indicates milder deceleration of the flow through the passage, which helps suppress boundary-layer growth and delay separation, thereby improving aerodynamic performance. The largest improvements occurred in configurations that initially exhibited strong shocks and pronounced wake deficits, with reductions in profile-loss coefficient of up for the most front-loaded baseline designs (e.g., Case1). In terms of the diffusion factor, it confirms smoother velocity recovery and reduced flow deceleration. For more balanced or aft-loaded baseline designs (e.g., Case3 and Case 4), the improvements were smaller in absolute magnitude but remained notable. In general, performance data confirm that curvature-controlled optimization is particularly effective in mitigating shock-induced losses. These results show the versatility of the approach and its potential as a valuable pre-design tool for developing new blades and retrofitting existing profiles.

5.2 Application cases of axial steam and gas turbine design and analysis

Building upon the validated numerical methodology and aerodynamic optimization strategy presented in Section 5.1, the complete blade design process, which comprised including preliminary 1D mean-line analysis, detailed 2D blade-section optimization, and full three-dimensional axial blade-row design, was applied to two representative turbomachinery cases to further demonstrate its applicability. The first is a high-pressure partial-admission axial steam turbine for marine waste-heat recovery, and the second is a low-pressure axial gas turbine in a turbofan engine for aerospace applications. These case studies demonstrate the transferability of the proposed approach across different working fluids, Mach number regimes, and geometric constraints.

5.2.1 High-pressure partial-admission axial steam turbine

This case study concerns a high-pressure partial-admission axial steam turbine integration into a cascade waste-heat recovery system carried by Climeon. In this system, the conventional steam turbine, that is, the Rankine cycle, is connected in series with the ORC unit to maximize the

utilization of waste heat.

Design procedure

Based on the specified inlet steam conditions and output requirements, the turbine stage was designed to meet constraints on compact geometry, simplified manufacturing, and cost-effectiveness. To satisfy these requirements, a constant-radius, single-stage configuration with partial-arc admission was adopted as a balanced compromise between aerodynamic efficiency and mechanical feasibility. This approach avoids the substantial endwall and secondary-flow losses that would otherwise arise from using very short blades at low mass flow rates, where high aspect ratios and increased viscous effects become significant. Although partial-arc admission introduces inlet non-uniformity and associated circumferential losses, the partial-admission degree was carefully optimized to minimize these effects.

1D mean-line design: A parametric study was conducted using a mean-line model to evaluate the effects of admission degree and total-to-static pressure ratio on stage efficiency. The results indicated a peak normalized efficiency at an admission degree of $\varepsilon = 0.4$, which was selected as the design value. Based on this analysis, the operating pressure ratio was set to 8.1, balancing aerodynamic performance and mechanical stress considerations, as illustrated in Figures 5.8. The final 1D design parameters are summarized in Table 5.1.

Table 5.1: One-dimensional supersonic, single-stage turbine design data.

Parameter	Stator	Rotor
Number of Blades	56	160
Admission Degree (ε)	0.4	0.48
Channel Height (const.) [m]	0.01	0.01
Mean Radius (const.) [m]	0.15	0.15
Blade Chord [m]	0.02	0.01
Inlet blade angle (relative) [°]	0	50
Outlet blade angle (relative) [°]	75	−42
Inlet wedge angle [°]	53	27
Outlet wedge angle [°]	3.7	12

2D profile design and optimization: The 1D mean-line results were imported into AxCent to optimize the blade profile curvatures. To achieve supersonic flow within the rotor passages, the blade channel geometry must adopt a converging–diverging configuration, enabling acceleration to supersonic speeds followed by controlled expansion. Given the supersonic nature

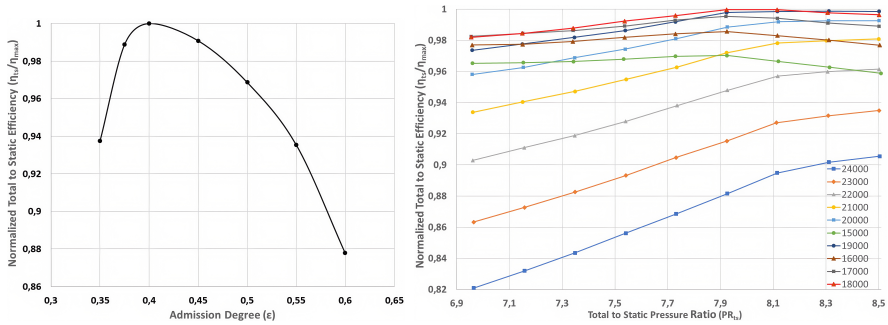

Figure 5.8: Influence of admission degree and total-to-static pressure ratio on normalized total-to-static efficiency.Normalized total-to-static efficiency as a function of admission degree (left). Influence of total-to-static pressure ratio on normalized total-to-static efficiency for different rotational speeds (right).

of the flow in the stator–rotor passages, shock control was a key design consideration: premature normal shocks in the stator channels can cause subsonic inflow to the rotor and reduce turbine efficiency, while shocks within the rotor passages introduce additional aerodynamic losses.

Blade-to-blade flow simulations revealed strong normal shocks along the suction side of the rotor blades, resulting in significant total-pressure losses (Figure 5.9, left). To address this, the rotor suction-side curvature was reshaped using a manual Bezier-curve optimization. The resulting profile replaced the strong normal shock with a weaker oblique shock (Figure 5.9, right), enabling smoother acceleration, which reduced the associated losses.

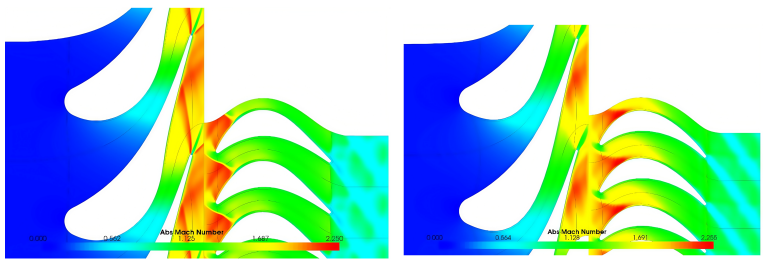

(a) Original Blade (a) Optimized Blade

Figure 5.9: Mach number contours at midspan for original (left) and optimized (right) rotor blade designs.

3D Flow Analysis: Full-annulus 3D simulations were conducted to evaluate the effects of partial admission under representative operating conditions. Figure 5.10 shows Mach number contours at midspan near the entrance of the blocked arc, while Figure 5.11 reveals elevated Mach numbers near the blade tips within the blocked arc, attributed to circumferential flow redistribution. The results indicate that the blocked sector induces

strong shocks and flow separation at the inlet of the admission arc, which propagate through several rotor passages. These shock waves are the primary sources of additional aerodynamic loss and contribute to unsteady loading on the rotor.

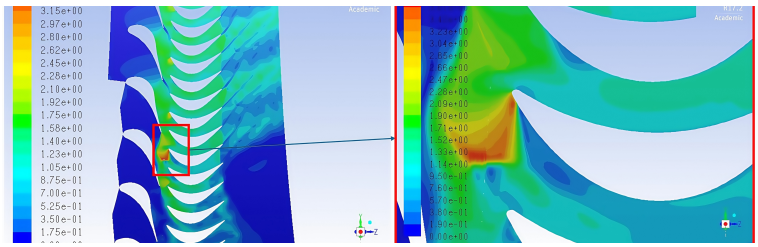

Figure 5.10: Contours of Mach number near the inlet side of the blockages, with a zoomed-in view highlighting the shock waves

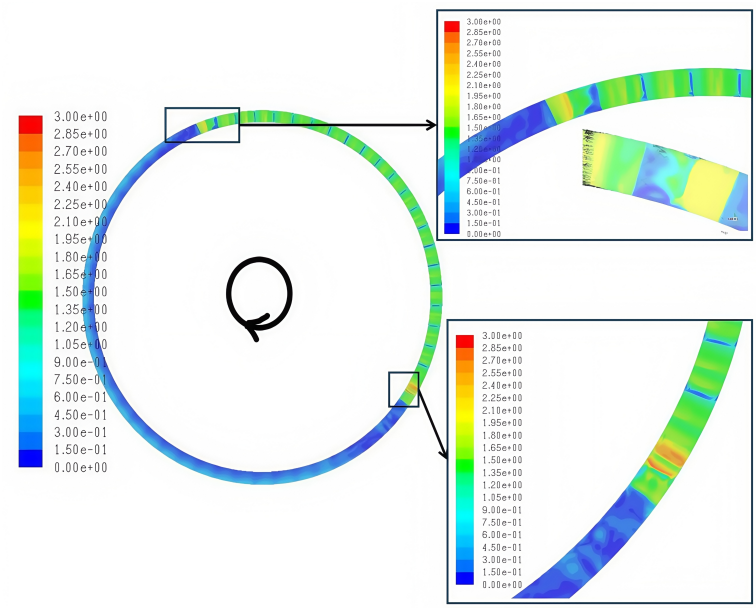

Figure 5.11: Contours of Mach number at the interface between stator and rotor, showing detailed flow structures at the inlet and outlet of the blocked arc.

To quantify the unsteady aerodynamic loads, the forces on the rotor blades were compared along the circumference. Figure 5.12 presents unsteady tangential forces on selected rotor blades, along with their projections in the X, Y, and Z directions. The direction of blade rotation is from higher to lower circumferential angles. The tangential force changes direction both at

the inlet and outlet sides of the blocked region; however, the inlet side exhibits the largest tangential force amplitudes. At the inlet, shock waves and steep velocity gradients generate strong fluctuations, while abrupt geometric changes and boundary-layer separation induce intense unsteady vortices that further amplify these fluctuations. In contrast, the outlet side shows milder and less pronounced force variations as the flow gradually recovers.

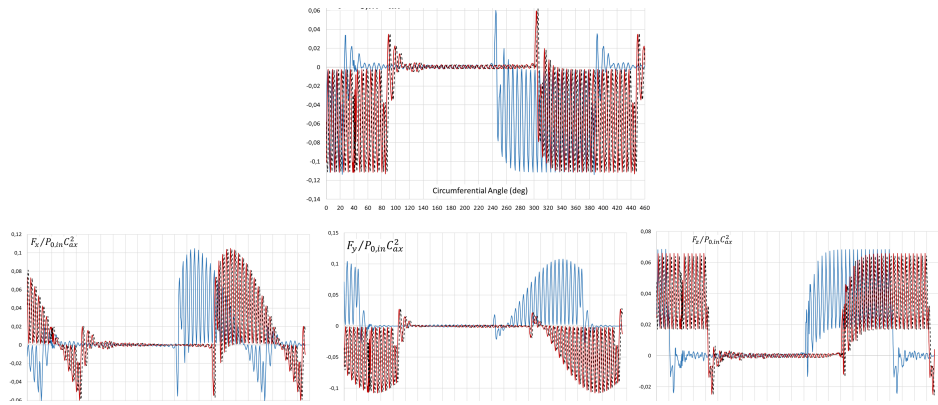

Figure 5.12: Comparison of unsteady aerodynamic force coefficients on the rotor blades for two configurations, plotted as a function of circumferential angle. Forces are normalized by $\rho_{0,\mathrm{in}} C_{\mathrm{ax}}^2$, where $\rho_{0,\mathrm{in}}$ is the inlet total density and C_{ax} is the axial velocity. Top: overall force variation; bottom row: (left) axial component F_x, (middle) tangential component F_y, (right) radial component F_z.

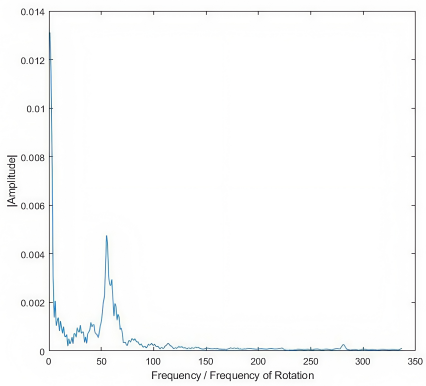

Figure 5.13: Fast Fourier Transform (FFT) of unsteady forces on rotor blades, showing amplitude as a function of frequency normalized by the rotational frequency. The dominant peak corresponds to the blade-passing frequency.

It is difficult to determine the force amplitude and frequency content directly from the time domain. Therefore, a Fast Fourier Transform (FFT) was applied to the unsteady forces for one of the rotor blades (Figure 5.13). The FFT results for the tangential force component indicate that the first

and second multiples of the rotation frequency have the highest amplitudes, owing to the single blockage and the change in tangential force direction at both sides of the blocked region. A distinct peak is also observed at the stator blade passing frequency (56 blades), caused by the intense shock waves. Combined time- and frequency-domain analyses reveal substantial unsteady forces that may lead to blade fatigue and wear during prolonged operation. Identifying the dominant excitation frequencies is crucial for avoiding resonance; by ensuring adequate separation between excitation and natural frequencies in the design phase, structural safety and durability can be significantly enhanced. In cases where the separation margin is insufficient, either design modifications should be implemented to shift the natural frequencies, or operational restrictions should be applied to avoid critical excitation ranges.

5.2.2 Characteristics of the LPT design

In the context of the RM400 geared turbofan engine, a comprehensive aerodynamic design and optimization is carried out for the LPT, with a particular focus on enhancing performance while addressing cooling challenges. The primary objective is to develop a highly loaded, low-reaction design that minimizes reliance on rotor cooling while maximizing aerodynamic efficiency. Drawing on established practices from high-pressure supersonic axial steam turbine development, the process progresses from one-dimensional mean-line calculations, through two-dimensional profile optimization, to three-dimensional flow-field analysis.

Design procedure

1D Mean-Line design: Based on the given operating and geometric constraints provided for the project, preliminary mean-line calculations were conducted in Concepts NREC AXIAL. Design points were established using the Smith chart in combination with empirical loss models (AMDC, KO, MK, and BSM). As shown in Figure 5.14, the mid-span reaction increases progressively from Stage 1 to Stage 3. The first-stage reaction is only 0.29, effectively reducing the rotor relative inlet temperature (RIT) and alleviating thermal stresses on the first-stage blades, while also reducing cooling requirements. In the subsequent stages, the reaction gradually increases, producing a smoother overall RIT distribution.

Meridional contour design: Following the mean-line design, the merid-

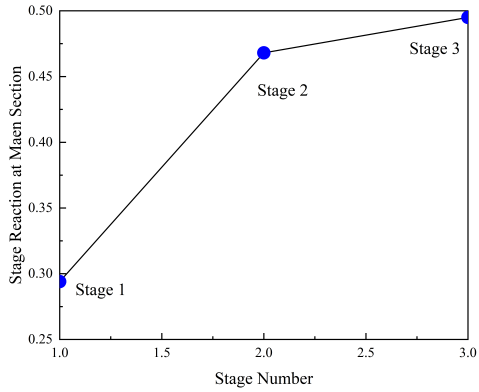

Figure 5.14: Stage reaction at mid-span for each of the three stages in the RM400 turbofan LPT design.

ional contour of the three-stage LPT was generated, as shown in Figure 5.15.

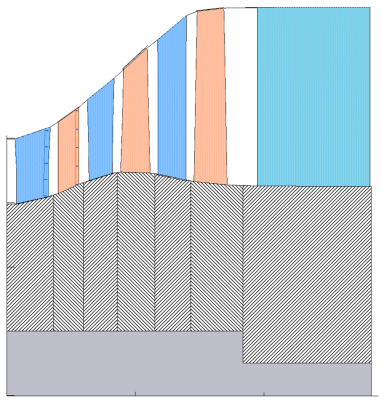

Figure 5.15: Meridional contour of the three-stage LPT.

The design features a hub-line "bump" shaped according to the area rule. The contraction at the first stage reduces the annulus area, accelerates the flow, and creates a favorable pressure gradient that suppresses boundary-layer separation and secondary-flow losses. This geometry also facilitates a smooth transition to the lower-loading downstream stages, helping maintain axial velocity uniformity and keeping inlet incidence and outlet relative Mach numbers within the desired range.

2D blade-to-blade optimization: The blade profiles were optimized in AxCent using the curvature-controlled Bezier-curve method, with constraints on throat location, outlet metal angle, and chord length. The

objective was to maintain a smooth isentropic Mach number distribution across the blade surfaces. Figures 5.16–5.18 show the isentropic Mach number contours at (a) 2%, (b) 57%, (c) 98%span for stage 1, 2 and 3.

In the Rel Mach number contours (Fig. 5.16), the peak relative Mach number increases radially from hub to tip, reaching its maximum at the tip (98% span) as circumferential speed U rises and the local degree of reaction increases. Stage 2 shows the same radial trend (Fig. 5.17), with a tip-region peak of approximately $M_{\text{rel}} \approx 1.3$, driven by the combined effects of higher blade speed and increased tip reaction. In Stage 3 (Fig. 5.18), no distinct shocks or separation zones are observed; the peak relative Mach number remains below ~ 1.15 at all spans (within the $M_{\text{is,max}} \leq 1.2$ target), and the normalized total-pressure contours $p_0/p_{0,\text{in}}$ are smooth, indicating low loss. The steepest increases in surface Mach number occur over $x/c \approx 0.6$–0.9, evidencing aft-loading that mitigates leading-edge overspeed and manages adverse pressure gradients toward the rear chord.

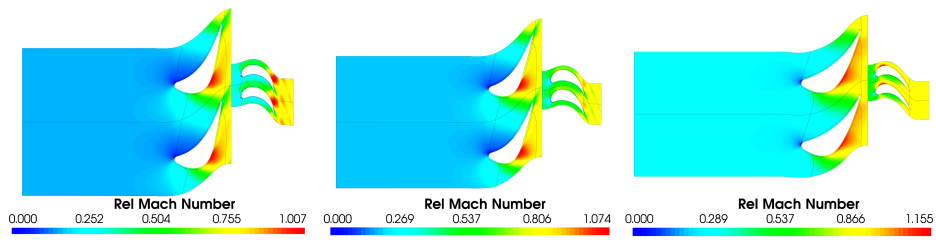

Figure 5.16: Contours of isentropic Mach number distribution at (a) 2%, (b) 57%, (c) 98%span for stage 1.

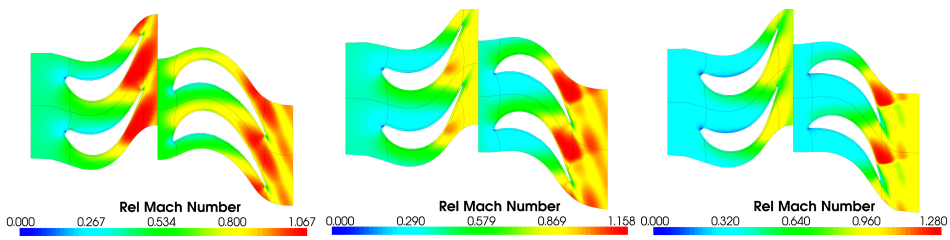

Figure 5.17: Contours of isentropic Mach number distribution at (a) 2%, (b) 57%, (c) 98%span for stage 2.

Figure 5.19 presents the isentropic relative Mach number distributions in Stage 1 for stator and rotor at 2%, 57%, and 98% span. At 2% span, the profile shows an impulse-type rise to a local peak near 15–20% chord (approximately 1.15) before decreasing, with most of the enthalpy drop in the stator and minimal rotor expansion. At 57% span, the distribution becomes bell-shaped with a reaction of 0.29, splitting the enthalpy drop

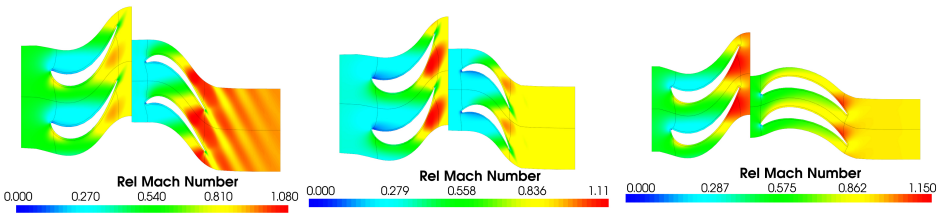

Figure 5.18: Contours of isentropic Mach number distribution at (a) 2%, (b) 57%, (c) 98%span for stage 3.

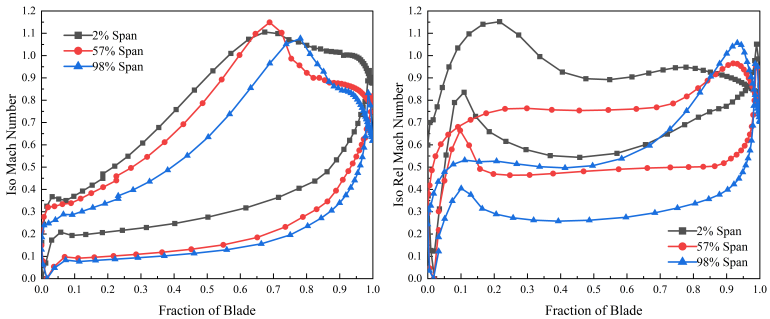

Figure 5.19: Isentropic relative Mach number distributions along the blade surfaces of the stator (left) and rotor (right) in Stage 1 at 2%, 57%, and 98% span.

between stator (approximately 70%) and rotor (approximately 30%). At 98% span, the trend shifts to reaction-type, with greater rotor expansion near the tip. The results indicate that, under the current reaction distribution in this stage, the isentropic Mach number on the rotor at 2% span reaches approximately 1.15, with the peak occurring relatively close to the leading edge.

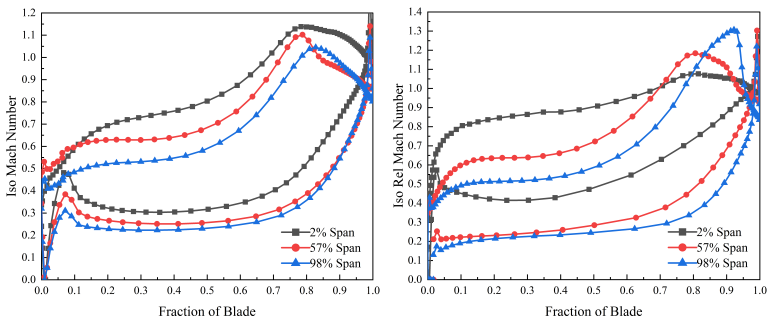

Figure 5.20: Isentropic relative Mach number distributions along the blade surfaces of the stator (left) and rotor (right) in Stage 2 at 2%, 57%, and 98% span.

Figure 5.20 shows the isentropic relative Mach number distributions in Stage 2 at 2%, 57%, and 98% span. At 2% span, the stator and rotor peak

at approximately 1.10 and 1.00, respectively, indicating higher loading on the stator. At 57% span, the smooth increase to about 1.20 reflects a balanced load split consistent with the 0.5 reaction design. At 98% span, reduced stator loading shifts more of the enthalpy drop to the rotor, yielding a tip peak of around 1.30, characteristic of high-reaction regions.

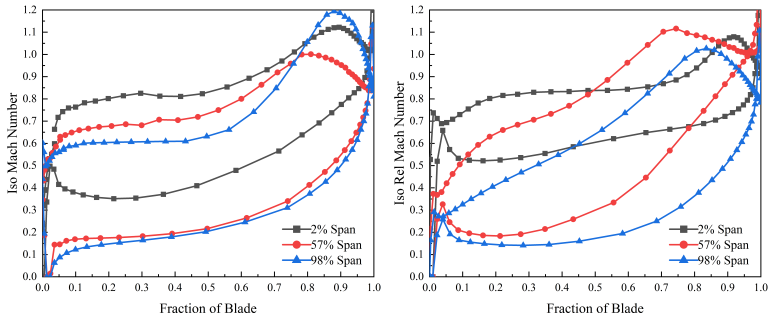

Figure 5.21: Isentropic relative Mach number distributions along the blade surfaces of the stator (left) and rotor (right) in Stage 3 at 2%, 57%, and 98% span.

Figure 5.21 shows trends similar to Stage 2, with uniformly distributed loading at 57% span and Mach numbers remaining below 1.2 at all spans. The aft-loaded profiles delay peak acceleration, helping maintain boundary-layer stability and avoid shock-induced losses—consistent with Stage 3 having the lowest stage loading and flow coefficient.

3D Flow Analysis: Following the 2D optimization, full-annulus steady 3D simulations were conducted to assess the aerodynamic performance of the LPT. Figure 5.22 shows the relative Mach number distributions at the blade hub (2% span), mid-span (57% span), and tip (98% span). In Stage 2, the stator shows its highest local relative Mach number at the hub, peaking at approximately 1.39. This produces a narrow suction-side shock band of about 3% chord length and a corresponding localized entropy rise. This behavior differs from the two-dimensional B2B results, in which the maximum peak 1.30 occurred at the rotor tip of Stage 2. The discrepancy arises because the three-dimensional full-annulus simulation resolves endwall secondary flows, spanwise blade-geometry variation, and local flow non-uniformities absent in the B2B method. In particular, secondary flows and hub-endwall boundary-layer growth cause an effective throat-area reduction near the stator hub, accelerating the local flow along the suction surface. This shifts the location of the maximum relative Mach number from the rotor tip (in 2D) to the stator hub (in 3D) and increases its magnitude from about 1.30 to 1.39.

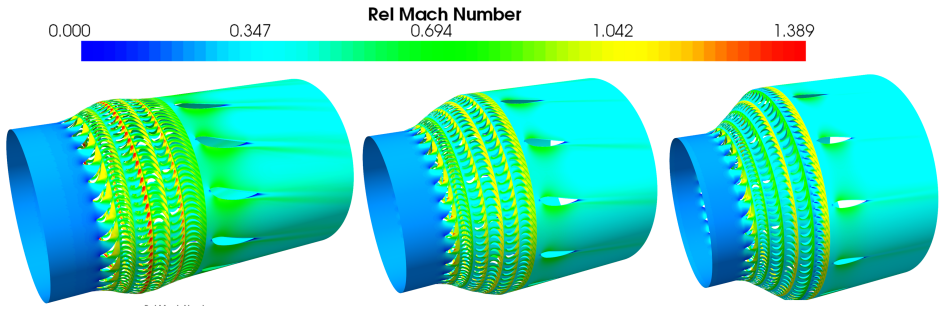

Figure 5.22: Contours of relative Mach number at 2%, 57%, and 98% span.

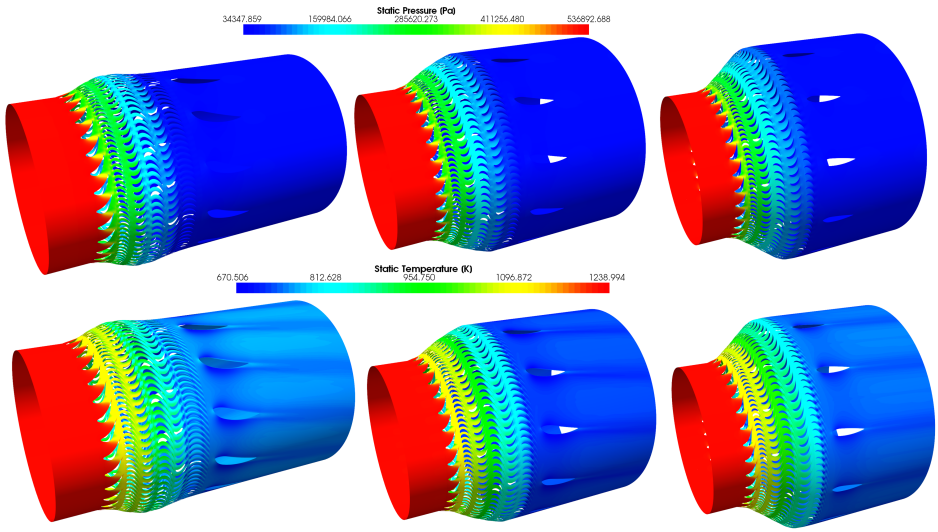

Figure 5.23: Contours of static pressure and static temperature at 2%, 57%, and 98% span. The first row depicts the static pressure contours, and the second row depicts the static temperature contours.

Figure 5.23 illustrates the static pressure (top row) and static temperature (bottom row) contours at three spanwise locations (2%, 57%, and 98%). The static pressure distributions show a progressive pressure drop in each stator-rotor row, consistent with the expansion process in the turbine. The pressure gradient is most pronounced near the hub (2% span), indicating stronger expansion in this region, while it becomes more gradual toward the tip (98% span). The static temperature contours reveal a corresponding temperature decrease as the flow passes through successive stages, reflecting the conversion of thermal energy into mechanical work. A more significant temperature drop is observed at the hub compared to the tip, in line with the spanwise reaction distribution and endwall effects.

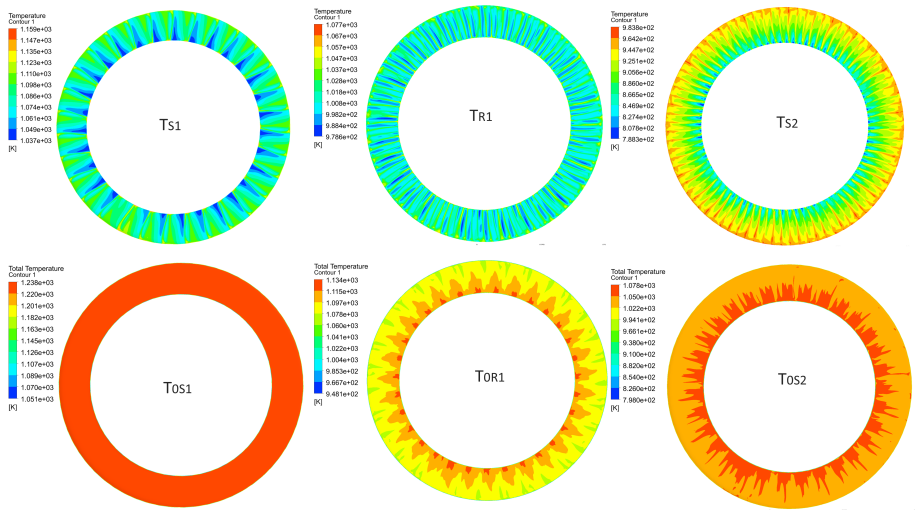

Figure 5.24: Temperature contours on an axial plane at turbine outlet.The top row shows static temperature contours at the first-stage stator (Ts1), first-stage rotor (Tr1), and second-stage stator (Ts2). The bottom row displays total temperature contours at the first-stage stator outlet (ToS1), first-stage rotor outlet (ToR1), and second-stage stator outlet (ToS2).

Figure 5.24 shows the distributions of static temperature (top row) and total temperature (bottom row) on an axial plane at the turbine outlet. As given condition, the static temperature at the inlet of the first-stage stator inlet is 1227K, The static temperature contours at Ts1 indicate that, at the exit of the first-stage stator, temperatures are approaching 1040 K. After passing through the rotor blades, the static temperature at the outlet (TR1) slightly decreases to around 998 K, implying a significant temperature drop from the stator exit to the rotor inlet and showing that the stator is responsible for most of the stage's temperature drop. In the Ts1 section, there is a clear temperature difference between the suction and pressure sides of the blades, indicating that the stator blades absorb most of the thermal energy inlet.

For total temperature, the total temperature at the inlet of the first-stage stator is 1230K. At the first-stage stator exit (ToS1), the total temperature remains nearly constant at about 1230K, showing negligible total temperature change through the stator. At the rotor exit (ToR1), the total temperature decreases to around 1090K. At the second-stage stator (ToS2), the total temperature is about 1080K. These results indicate that the total temperature is essentially unchanged across the stator passages, while it decreases monotonically through the rotors due to work extraction. Meanwhile, ToS1 exhibits almost no circumferential temperature fluctuations,

meaning that the total temperature at the stator exit becomes uniformly distributed.

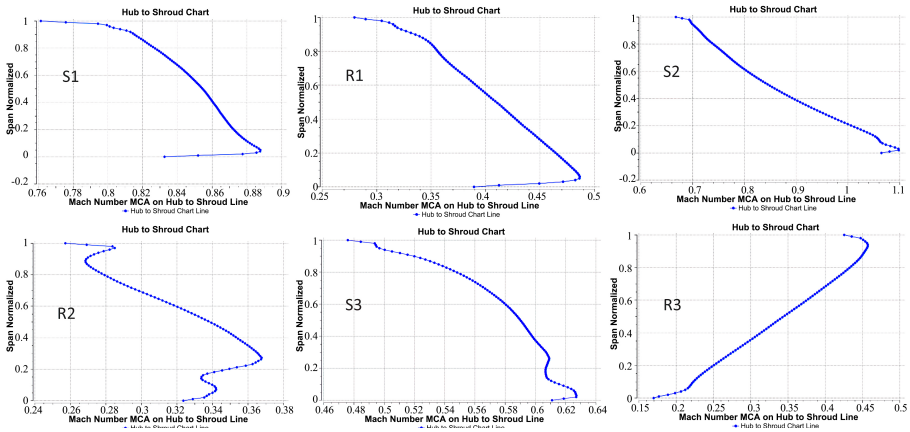

Figure 5.25: Circumferentially mass-averaged Mach number vs. nondimensional blade span at various Sections along domain.S1 represents sections between stator 1 and rotor 1, R1 represents sections between rotor 1 and stator 2, S2 represents sections between stator 2 and rotor 2, R2 represents sections between rotor 2 and stator 3,S3 represents sections between stator 3 and rotor 3, R3 represents sections between rotor 3 and OGV.

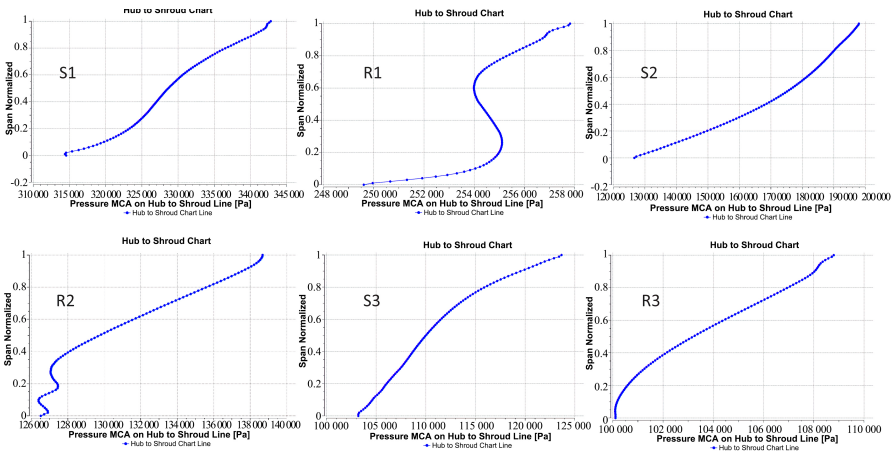

Figure 5.26: Circumferentially mass-averaged Static pressure vs. nondimensional blade span at various Sections along domain.

Figures 5.25 and 5.26 show circumferentially mass-averaged Mach number and static pressure distributions, respectively, along the nondimensional blade span for sections between each stator and rotor (S1, R1, S2, R2, S3, R3). Stage 1 displays pronounced Mach number oscillations and localized static-pressure dips in the hub region near R1, suggesting strong flow non-uniformities possibly associated with shock–boundary-layer interactions and secondary-flow effects. Stage 2 exhibits smooth flow with effec-

tive pressure recovery, confirming the benefits of the mid-reaction design, although a Mach peak near the hub highlights an entropy hotspot. Stage 3 maintains stable low-loading characteristics favorable for high efficiency.

From a design perspective, the three-stage LPT achieves its primary objective of a low-reaction first stage. However, two key sources of loss remain: spanwise non-uniformity and localized tip deceleration in R1, as well as shock-wave-induced losses in the second-stage blades. Future improvements should focus on R1 through hub/tip profiling, endwall contouring, and minor stagger adjustments, and on Stage 2 through a targeted number of stages, stagger, and curvature refinements to reduce residual shock effects. tion LPT, which combines high efficiency with reduced cooling complexity.

Chapter 6

Summary and outlook

6.1 Summary

This thesis has presented the development and application of an integrated workflow for high-efficiency axial turbine design. The workflow combines empirical loss models, curvature-controlled blade parameterization, and advanced CFD techniques into a reproducible "1D $\rightarrow$ 2D $\rightarrow$ 3D" design chain. The approach was validated through two representative case studies: a supersonic partial-admission steam turbine and a low-pressure gas turbine.

The main contributions of this work are:

- **End-to-End Design Process:** Established a complete process linking mean-line analysis, 2D blade-to-blade optimization, and 3D full-annulus simulations, ensuring consistent aerodynamic principles from concept through final verification.
- **Validated aerodynamic predictions:** Demonstrated close agreement between CFD predictions and experimental measurements for the reference blade cases, confirming the reliability of the SST k–ω RANS model and the adopted numerical setup.
- **Curvature-controlled blade optimization:** Developed a Bezier-curve-based parameterization framework within the optimization process, enabling precise control of local curvature and loading distribution. The resulting designs reduced shock strength, suppressed separation, and lowered profile losses.

- **Performance enhancement in industrial configurations:** Applied the workflow to a single-stage steam turbine and a three-stage low-pressure gas turbine, achieving measurable aerodynamic improvements through optimized curvature distribution and reduced losses.

6.2 Outlook

While the proposed workflow has proven effective, several opportunities remain for further improvement:

- **Multi-physics and structural coupling:** Coupling aerodynamic optimization with thermal and structural analyses would enable simultaneous enhancement of efficiency, durability, and mechanical integrity.
- **High-fidelity unsteady simulations:** Expanding the use of LES/DES for selected operating points could provide deeper insights into unsteady shock–boundary-layer interactions, especially in partial-admission and transonic regimes.
- **Automated multi-objective optimization:** Incorporating surrogate modeling and genetic algorithms could accelerate the search for designs that balance efficiency, stability, and manufacturing constraints.

References

[1] D. G. Wilson. *The Design of High-Efficiency Turbomachinery and Gas Turbines*. MIT Press, Cambridge, MA, 1st edition, 1989.

[2] M. P. Boyce. *Gas Turbine Engineering Handbook*. Gulf Publishing Company, Houston, TX, 1st edition, 1982.

[3] GE Power. Steam power plant turbine systems. Available:https://www.ge.com/power/, 2023. Accessed: 2024-05-29.

[4] Rolls-Royce. Aircraft engines. Available:https://www.rolls-royce.com/products-and-services/civil-aerospace.aspx, 2023. Accessed: 2024-05-29.

[5] NOAA Marine Operations. Marine propulsion systems. Available: https://www.omao.noaa.gov/, 2023. Accessed: 2024-05-29.

[6] M. P. Boyce. *Gas Turbine Engineering Handbook*. Butterworth–Heinemann, Oxford, UK, 3rd edition, 2012.

[7] H. I. H. Saravanamuttoo, G. F. C. Rogers, and H. Cohen. *Gas Turbine Theory*. Pearson Education, Harlow, UK, 5th edition, 2001.

[8] J. D. Anderson. *Computational Fluid Dynamics: The Basics with Applications*. McGraw-Hill, New York, NY, USA, 1st edition, 2002.

[9] A. Poullikkas. An overview of current and future sustainable gas turbine technologies. *Renewable and Sustainable Energy Reviews*, 9 (5):409–443, 2005.

[10] A. I. Turja, I. A. Khan, S. Rahman, A. Mustakim, M. I. Hossain, M. M. Ehsan, and Y. Khan. Machine learning–based multi-objective optimization and thermal assessment of supercritical co2 rankine cycles for gas turbine waste heat recovery. *Energy and AI*, 16:100372, 2024.

[11] A. H. Elsheikh, S. W. Sharshir, M. Elaziz, A. Kabeel, G. Wang, and H. Zhang. Modeling of solar energy systems using artificial neural network: A comprehensive review. *Solar Energy*, 180:622–639, 2019.

[12] T. Debroy, H. L. Wei, J. Zuback, T. Mukherjee, and W. Zhang. Additive manufacturing of metallic components – process, structure and properties. *Progress in Materials Science*, 92:112–224, 2018.

[13] A. Singh and D. Sharma. Efficiency enhancement in turbomachinery: Bridging numerical modeling and experimental validation for fluid dynamics advancements. *Journal of Sustainable Urban Futures*, 13 (9):1–15, 2023.

[14] S. Gülen and M. Curtis. Gas turbine's role in energy transition. *Journal of Engineering for Gas Turbines and Power*, 146(10):–, 2024.

[15] N. Yao, W. Pan, J. Zhang, and L. Wei. The advancement on carbon-free ammonia fuels for gas turbine: A review. *Energy Conversion and Management*, 315:118745, 2024.

[16] M. Pietropaoli, R. Ahlfeld, F. Montomoli, A. Ciani, and M. D'Ercole. Design for additive manufacturing: Internal channel optimization. *Journal of Engineering for Gas Turbines and Power*, 139(10):102101, 2017.

[17] O. P. Sharma and T. L. Butler. Predictions of endwall losses and secondary flows in axial flow turbine cascades. In *Proceedings of the ASME International Gas Turbine Conference and Products Show*, page V001T01A098, 1986.

[18] M. A. Rezaienia and T. Korakianitis. High-loaded axial turbines: Aerodynamic challenges and optimization strategies. *Journal of Turbomachinery*, 142(7):071008, 2020.

[19] R. W. Ainsworth and Others. Advances in high-performance axial turbine design for next-generation applications. *ASME Turbo Expo*, pages GT2021–59184, 2021.

[20] Y. Li, W. Xue, L. Luo, H. Yan, W. Du, Q. Luo, and S. Yang. Influence of a novel leading-edge winglet on the aerodynamic characteristics of a highly loaded turbine. *Aerospace Science and Technology*, 152: 109301, 2024.

[21] S. Bouterra, R. Belamadi, A. Djemili, and A. Ilinca. Flow separation control and aeroacoustic effects of a leading-edge slat over a wind turbine blade. *Energies*, 17(22):5597, 2024.

[22] O. Schennach, R. Pecnik, B. Paradiso, E. Göttlich, A. Marn, and J. Woisetschläger. The effect of vane clocking on the unsteady flowfield in a one and a half stage transonic turbine. *Turbo Expo: Power for Land, Sea, and Air*, 47950:793–802, 2007.

[23] S. Lardeau and P. Tucker. Optimized endwall contouring for high-loading axial turbine blades. *Journal of Propulsion and Power*, 38 (1):101–114, 2022.

[24] L. Zhang and H. Xu. Three-dimensional design strategies for secondary flow control in axial turbines. *Aerospace Science and Technology*, 111:106556, 2021.

[25] J. Martinez and Colleagues. Additive manufacturing applications in turbomachinery blade design. *Additive Manufacturing*, 28:78–90, 2019.

[26] X. Huang and C. Zhou. Advanced manufacturing and blade aerodynamic optimization: Recent progress and perspectives. *Energy Conversion and Management*, 284:116849, 2023.

[27] W. Lee and P. Gielski. Robust turbine blade design across variable operating conditions. *International Journal of Turbo & Jet Engines*, 37(2):145–159, 2020.

[28] H. F. S. Lui, T. R. Ricciardi, W. R. Wolf, J. Braun, I. Rahbari, and G. Paniagua. Unsteadiness of shock–boundary layer interactions in a mach 2.0 supersonic turbine cascade. *Physical Review Fluids*, 7(9): 094602, 2022.

[29] A. Mahmoudi, M. Fazli, and M. R. Morad. A recent review of waste heat recovery by organic rankine cycle. *Applied Thermal Engineering*, 143:660–675, 2018.

[30] T.-C. Hung, T.-Y. Shai, and S. K. Wang. A review of organic rankine cycles (orcs) for the recovery of low-grade waste heat. *Energy*, 22(7): 661–667, 1997.

[31] Y. Dai, J. Wang, and L. Gao. Parametric optimization and comparative study of organic rankine cycle (orc) for low grade waste heat recovery. *Energy Conversion and Management*, 50(3):576–582, 2009.

[32] N. Nazari, P. Heidarnejad, and S. Porkhial. Multi-objective optimization of a combined steam-organic rankine cycle based on exergy and exergo-economic analysis for waste heat recovery application. *Energy Conversion and Management*, 127:366–379, 2016.

[33] J. R. Seume, M. Peters, and H. Kunte. Design and test of a 10 kw orc supersonic turbine generator. *Journal of Physics: Conference Series*, 821:012023, 2017.

[34] G. Paniagua, M. C. Iorio, N. Vinha, and J. Sousa. Design and analysis of pioneering high supersonic axial turbines. *International Journal of Mechanical Sciences*, 89:65–77, 2014.

[35] S. Rashid, M. Tremmel, J. Waggott, and R. Moll. Curtis stage nozzle/rotor aerodynamic interaction and the effect on stage performance. In *Turbo Expo: Power for Land, Sea, and Air*, volume 4241, pages 937–948, 2006.

[36] R. Ghio, C. Raffaeli, A. Sabattini, V. Dossena, A. Fusetti, A. Spinelli, C. Osnaghi, F. Cozzi, and Others. Experimental and numerical analysis of supersonic blade profiles developed for highly loaded impulse type steam turbine stages. In *12th European Conference on Turbomachinery Fluid Dynamics and Thermodynamics, ETC 2017*, pages 1–13, 2017.

[37] J. E. Fridh, B. Bunkute, R. Fakhrai, and T. Fransson. An experimental study on partial admission in a two-stage axial air test turbine with numerical comparisons. In *Proceedings of the ASME Turbo Expo 2004*, pages 1285–1297, 2004.

[38] X. Shen and T. Korakianitis. Effects of continuous surface curvature on axial compressor blade performance. *Journal of Turbomachinery*, 141(10):101008, 2019.

[39] Y. Song and C. Gu. Numerical and theoretical investigations concerning surface curvature effects in compressor blades. *Energies*, 13 (7):1767, 2020.

[40] I. A. Hamakhan and T. Korakianitis. Aerodynamic performance effects of leading-edge geometry in gas-turbine blades. *Applied Energy*, 87(5):1591–1601, 2010.

[41] K. Siddappaji, M. G. Turner, and A. Merchant. General capability of parametric 3d blade design tool for turbomachinery. In *Turbo Expo: Power for Land, Sea, and Air*, volume 44748, pages 2331–2344, 2012.

[42] T. P. Korakianitis. Design of airfoils and cascades of airfoils. *AIAA Journal*, 27(4):455–461, 1989.

[43] A. M. Elewe. Numerical simulation of surface curvature effect on aerodynamic performance of different types of airfoils. In *IOP Conference Series: Materials Science and Engineering*, volume 928, page 032003, 2020.

[44] T. Korakianitis and M. Rezaienia. Prescribed surface curvature method for advanced turbine blade design. *Journal of Engineering for Gas Turbines and Power*, 143(12):121001, 2021.

[45] W. Guo and F. Zhang. Machine learning–assisted optimization of surface curvature for gas turbine blades. *Applied Energy*, 288:116653, 2021.

[46] H. Wu and Z. Li. Artificial intelligence–based aerodynamic shape optimization of turbomachinery blades. *Energy Reports*, 8:1359–1370, 2022.

[47] J. Park and H. Kim. Mitigation of secondary flows through curvature-controlled blade design. *Aerospace Science and Technology*, 114: 106678, 2021.

[48] R. Sandberg and V. Michelassi. Assessment of rans capabilities for predicting loss mechanisms in turbine cascades. *Journal of Turbomachinery*, 141(7):071009, 2019.

[49] L. Fu and Z. Wang. Validation of rans simulations for highly loaded axial turbine blades. *Aerospace Science and Technology*, 98:105686, 2020.

[50] V. Michelassi and R. Pichler. Hybrid rans-les simulation of secondary flow development in a high-pressure turbine. *Flow, Turbulence and Combustion*, 103(3):663–684, 2019.

[51] D. Bogojevic and O. Sharma. High-fidelity simulation of turbine blade row interactions using hybrid rans-les methods. *Journal of Propulsion and Power*, 37(4):540–552, 2021.

[52] W. Zhang and X. Li. Anisotropic grid strategies for turbomachinery flow simulations. *Computers & Fluids*, 201:104451, 2020.

[53] K. Hillewaert and J. Bodart. Time-accurate simulation of wake–blade interactions in axial turbines. *Journal of Turbomachinery*, 143(5): 051005, 2021.

[54] X. Zhao and Q. Yuan. Adjoint-based shape optimization for turbine blades using unsteady cfd. *Journal of Thermal Science*, 32(2):471–483, 2023.

[55] S. L. Dixon and C. A. Hall. *Fluid Mechanics and Thermodynamics of Turbomachinery*. Butterworth–Heinemann, Oxford, UK, 5th edition, 1998.

[56] H. I. H. Saravanamuttoo, G. F. C. Rogers, and H. Cohen. *Gas Turbine Theory*. Pearson Education, Harlow, UK, 5th edition, 2001.

[57] M. P. Boyce. Gas turbine engineering handbook. In *Gas Turbine Engineering Handbook*, chapter Sections 929–956, pages 721–768. Butterworth–Heinemann, Oxford, 3rd edition, 2012.

[58] B. Lakshminarayana. *Fluid Dynamics and Heat Transfer of Turbomachinery*. John Wiley & Sons, Inc., New York, 1st edition, 1995.

[59] J. L. Kerrebrock. *Aircraft Engines and Gas Turbines*. The MIT Press, Cambridge, MA, 1977.

[60] D. Japikse and N. C. Baines. *Introduction to Turbomachinery*. Concepts ETI, Inc., Redmond, WA, 1994.

[61] J. H. Horlock. *Axial Flow Turbines*. Butterworths & Co. Publishers Ltd, London, UK, 1st edition, 1966.

[62] H. Moustapha, M. F. Zelesky, N. C. Baines, and D. Japikse. *Axial and Radial Turbines*. Academic Press, Boston, 2021. ISBN 9780128207396.

[63] H. Cohen, G. F. C. Rogers, and H. I. H. Saravanamuttoo. *Gas Turbine Theory*. Longman Scientific and Technical, Harlow, UK, 1st edition, 1987.

[64] R. J. Latimer. *Axial Turbine Performance Prediction*. VKI Lecture Series 1978-2, 1978.

[65] N. Baines. *Turbine Blade Design: Technology and Practice*. Cranfield University Press, Cranfield, UK, 2019. ISBN 9781873736062.

[66] S. F. Smith. A simple correlation of turbine efficiency. *Journal of Royal Aero Soc*, 69:467–470, 1965.

[67] Y. A. Çengel and M. A. Boles. *Thermodynamics: An Engineering Approach*. McGraw-Hill Education, 8th edition, 2015.

[68] M. J. Moran and H. N. Shapiro. *Fundamentals of Engineering Thermodynamics*. John Wiley & Sons, Hoboken, NJ, USA, 7th edition, 2010.

[69] W. J. Kearton and H. P. Hodson. Incidence loss and deviation in turbine blades. *Proceedings of the Institution of Mechanical Engineers, Part A*, 199:157–168, 1985.

[70] R. H. Aungier. *Turbine Aerodynamics*. Concepts ETI, Redmond, WA, USA, 1st edition, 2006.

[71] D. Japikse and N. C. Baines. *Introduction to Turbomachinery*. Concepts ETI, Inc., Wilder, VT, USA, 1st edition, 1994.

[72] F. Lehhaus. Experimentelle untersuchungen an einem gasturbinenlaufrad-gitter mit dem schaufelprofil vk11. Technical Report Report No. 25 174 A, Deutsche Forschungs- und Versuchsanstalt für Luft- und Raumfahrt (DFVLR), Göttingen, Germany, Göttingen, Germany, 1975.

[73] O. Zweifel. The spacing of turbomachine blading, especially with large angular deflection. *Brown Boveri Review*, 32(12):436–444, 1945.

[74] J. Denton. Loss mechanisms in turbomachinery. *Journal of Turbomachinery*, 115(4):621–656, 1993.

[75] N. A. Cumpsty. *Jet Propulsion: A Simple Guide to the Aerodynamic and Thermodynamic Design and Performance of Jet Engines*. Cambridge University Press, 2nd edition, 2003.

[76] J. H. Dunham and P. G. Came. Turbine blade losses—laminar and turbulent flow. In *ASME Turbo Expo 1978*, 1978. Paper 78-GT-98.

[77] J. D. Denton. Endwall loss mechanisms in axial turbines. *Journal of Turbomachinery*, 112(2):195–203, 1990.

[78] N. A. Cumpsty and A. L. Heyes. Tip clearance flow and losses in axial turbine cascades. *Journal of Turbomachinery*, 101(1):1–8, 1979.

[79] J. H. Dunham and P. G. Came. Shock and transonic losses in high-speed turbines. *ASME Journal of Engineering for Power*, 100(3): 409–416, 1978.

[80] W. Traupel. Partial admission effects in turbine stages. In *Proceedings of the International Gas Turbine Conference*, pages 287–294. ASME, 1968.

[81] C. R. Soderberg. Empirical loss correlations for whole-blade performance. *Journal of Mechanical Engineering Science*, 1(4):220–226, 1952.

[82] D. G. Ainley and G. C. R. Mathieson. A method of performance estimation of axial-flow turbines. Reports and Memoranda 2974, Aero Research Council, London, UK, 1951.

[83] S. C. Kacker and U. Okapuu. A mean line prediction method for axial flow turbine efficiency. *Trans ASME Journal Engineering for Power*, 104:111–119, 1982.

[84] S. H. Moustapha, W. E. Carscallen, and J. D. McGeachy. Aerodynamic performance of a transonic low aspect ratio turbine nozzle. *Trans ASME Journal Turbomachinery*, 115:400–408, 1993.

[85] J. Dunham. A review of cascade data on secondary losses in turbines. *Journal of Mechanical Engineering Science*, 12:48–59, 1970.

[86] H. R. M. Craig and H. J. A. Cox. Performance estimation of axial flow turbines. *Proc Inst Mech Engrs*, 185:407–424, 1970.

[87] J. Dunham and P. M. Came. Improvements to the ainley-mathieson method of turbine performance prediction. *Trans ASME Journal Engineering for Power*, 92:252–256, 1970.

[88] S. H. Moustapha, S. C. Kacker, and B. Tremblay. An improved incidence losses prediction method for turbine airfoils. *Trans ASME Journal Turbomachinery*, 112:267–276, 1990.

[89] E. P. Vash, S. Giergis, and S. H. Moustapha. The design and performance of a high work research turbine. *Trans. ASME Journal of Turbomachinery*, 118:792–799, 1996.

[90] J. D. J. Anderson. *Modern Compressible Flow: With Historical Perspective*. McGraw-Hill, New York, NY, USA, 2nd edition, 1984.

[91] Y. S. Mamaev. Diffusion factors and flow separation in turbine blade cascades. *Journal of Turbomachinery*, 105:23–28, 1983.

[92] N. C. Baines and K. Nandakumar. *Aerodynamics of Turbomachinery*. Longman Scientific & Technical, 1988.

[93] V. Sarohia and J. P. Moore. Boundary-layer transition on turbine blades. *Journal of Engineering for Power*, 91(3):264–270, 1969.

[94] H. Schlichting and K. Gersten. *Boundary-Layer Theory*. Springer, Cham, Switzerland, 9th edition, 2016.

[95] Concepts NREC. *Turbomachinery Loss Models and Optimization User Guide*. Concepts NREC, Woburn, MA, USA, 2018. Accessed: 2024-05-29.

[96] R. E. Bensow and O. Soderlind. Multi-objective optimization of airfoil sections using curvature-based parameterization. In *ASME Turbo Expo*, 2013.

[97] M. A. Alves and J. S. Bower. Parameterization techniques for aerodynamic optimization. *AIAA Journal*, 42(8):1619–1628, 2004.

[98] H. Sobiczewski. Inverse design of axial turbomachinery blades for target mach number distributions. *International Journal of Turbo & Jet-Engines*, 8:93–107, 1991.

[99] J. Lieblein. Cascade airfoil diffusion factor and design criteria. Technical Report NASA TN D-4394, NASA Lewis Research Center, Cleveland, OH, USA, 1970.

[100] S. L. Dixon and C. A. Hall. *Fluid Mechanics and Thermodynamics of Turbomachinery*. Butterworth–Heinemann, Oxford, UK, 6th edition, 2014.

[101] W. Traupel and J. Petzold. Airfoil stacking methods for axial turbines. *ASME Journal of Engineering for Power*, 92(2):121–128, 1970.

[102] J. Mendoza and P. Schiavone. Meridional stacking strategies for improved aerodynamic performance. In *ASME Turbo Expo*, Glasgow, Scotland, 2010.

[103] F. M. White. *Fluid Mechanics*. McGraw-Hill, New York, NY, USA, 7th edition, 2011.

[104] S. B. Pope. *Turbulent Flows*. Cambridge University Press, Cambridge, UK, 2000.

[105] D. C. Wilcox. *Turbulence Modeling for CFD*. DCW Industries, La Cañada, CA, USA, 3rd edition, 2006.

[106] P. R. Spalart and S. R. Allmaras. A one-equation turbulence model for aerodynamic flows. *AIAA Journal*, 30(5):729–737, 1992.

[107] *ANSYS Fluent User's Guide*. ANSYS, Inc., Canonsburg, PA,USA, 2023 r1 edition, 2023. Accessed: 2024-05-29.

[108] *ANSYS CFX User's Guide*. ANSYS, Inc., Canonsburg, PA, USA, 2023 r1 edition, 2023. Accessed: 2024-05-29.

Summary of publications

Author contributions

Paper I: Numerical analysis of an axial high-pressure partial admission turbine

I simulated the internal flow characteristics of the supersonic turbine stages using CFD, optimized the rotor to improve performance, processed the resulting data, and carried out the writing, review, and editing. Narmin Hushmandi and Magnus Genrup provided technical suggestions, gave feedback, and proofread the paper.

Paper II: Numerical investigation on performance of gas turbine blade: effects of simulation models and blade geometry

I conducted the investigation and methodology, performed the CFD simulations, processed and analyzed the data, and carried out the writing, review, and editing.

Paper III: Numerical investigation on performance of a family of curvature distributions of gas turbine blades

I conducted the investigation and methodology, performed the CFD simulations and optimization, processed and analyzed the data, and carried out the writing, review, and editing. Narmin Hushmandi assisted with formatting and grammar checks, and Magnus Genrup provided technical suggestions, gave feedback, and proofread the paper.

Paper IV: Fundamental flow-path design for geared low-pressure turbines – aspects of cooling

I performed the CFD simulations and optimization, processed and analyzed the data, and carried out the writing, review, and editing. Narmin Hush-

mandi assisted with formatting and grammar checks, and Magnus Genrup provided technical suggestions, gave feedback, and proofread the paper.

Printed by Media-Tryck, Lund 2025 NORDIC SWAN ECOLABEL 3041 0903

Faculty of Engineering
Department of Energy Sciences

ISBN 978-91-8104-579-6
ISSN 0282-1990
ISRN LUTMDN/TMHP-25/1184